An unstructured finite volume method for coupled models of suspended sediment and bed-load transport in shallow water flows

Fayssal Benkhaldoun[*], Imad Elmahi[†], Saïda Sari[‡], Mohammed Seaïd[§]

Abstract

The aim of this work is to develop a well-balanced finite volume method for the accurate numerical solution of the equations governing suspended sediment and bed-load transport in two-dimensional shallow water flows. The modelling system consists of three coupled model components: (i) the shallow water equations for the hydrodynamical model, (ii) a transport equation for the dispersion of suspended sediments, and (iii) an Exner equation for the morphodynamics. These coupled models form a hyperbolic system of conservation laws with source terms. The proposed finite volume method consists of a predictor stage for the discretization of gradient terms and a corrector stage for the treatment of source terms. The gradient fluxes are discretized using a modified Roe's scheme using the sign of the Jacobian matrix in the coupled system. A well-balanced discretization is used for the treatment of source terms. In this paper, we also describe an adaptive procedure in the finite volume method by monitoring the concentration of suspended sediments in the computational domain during its transport process. The method uses unstructured meshes, incorporates upwinded numerical fluxes and slope limiters to provide sharp resolution of steep sediment concentrations and bed-load gradients that may form in the approximate solutions. Details are given on the implementation of the method, and numerical results are presented for two idealized test cases which demonstrate the accuracy and robustness of the method and its applicability in predicting dam-break flows over erodible sediment beds. The method is also applied to a sediment transport problem in the Nador lagoon.

Keywords. Suspended sediment; shallow water equations; bed-load transport; finite volume method; unstructured grids; mesh adaptation; Nador lagoon

1 Introduction

Mathematical modelling of suspended sediment and bed-load transport in shallow water flows is based on the formulation and solution of the appropriate equations of continuity and motion of water, sediments and bed-load. In general, hydrodynamical flows represent a three-dimensional turbulent Newtonian flow in complicated geometrical domains. The costs of incorporating three-dimensional data in natural water courses is often excessively high. Computational efforts needed to simulate three-dimensional turbulent flows can also be significant. In view of such considerations, many researchers have tended to use rational approximations in order to develop two-dimensional hydrodynamical models for water flows. Indeed, under the influence of gravity, many free-surface water flows can be modelled by the shallow water equations with the assumption that the vertical scale is much smaller than any typical horizontal scale. These equations can be derived from the depth-averaged incompressible Navier-Stokes equations using appropriate free-surface and boundary conditions along

[*]LAGA, Université Paris 13, 99 Av J.B. Clement, 93430 Villetaneuse, France (fayssal@math.univ-paris13.fr)

[†]ENSAO, EMSN, Université Mohammed 1, B.P. 669, 60000 Oujda, Morocco (ielmahi@ensa.ump.ma)

[‡]LAGA, Université Paris 13, 99 Av J.B. Clement, 93430 Villetaneuse, France (sari@math.univ-paris13.fr)

[§]School of Engineering and Computing Sciences, University of Durham, South Road, Durham DH1 3LE, UK (m.seaid@durham.ac.uk)

with a hydrostatic pressure assumption. The shallow water equations in depth-averaged form have been successfully applied to many engineering problems and their application fields include a wide spectrum of phenomena other than water waves. For instance, the shallow water equations have applications in environmental and hydraulic engineering such as tidal flows in an estuary or coastal regions, rivers, reservoir and open channel flows, see [1, 35] among others. In general, suspended sediments and bed-load transport in shallow water flows is determined by the characteristics of the hydraulics flow and the properties of the suspended sediments. Thus, dynamics of the water and dynamics of the sediments must be studied using a mathematical model made of three different but dependent model variables: (i) a set of hydraulics variables defining the dynamics of the water flow, (ii) a sediment variable defining the transport and dispersion of the sediments and (iii) a topography variable defining the dynamics of the bed-load. The model presented in this study includes the shallow water equations for the hydrodynamics, a transport equation for the conservation of sediment concentration, Exner equation for the morphodynamics, and empirical functions for bed friction, substrate erosion and deposition. Similar coupled sediment transport in free-surface water flow models have been developed in [14, 13, 12, 33] and the references therein. The model here differs from these in that (i) it accounts for movable beds using an Exner-type equation for the bed-load and (ii) it can be applied both to short time scales where the flow, sediment transport and morphodynamics evolution are strongly coupled and the rate of bed evolution is comparable to the rate of flow evolution (*e.g.*, erosion and deposition related to dam-break flows as those considered in the current work), or to relatively long time scales where the time scale of bed evolution associated with erosion and/or deposition is slow relative to the response of the flow to the changing water surface and therefore the classical quasi-steady approximation can be invoked (*e.g.*, erosion due to overland flows driven by steady water flows). The governing equations form a two-dimensional nonlinear hyperbolic system of conservation laws with source terms. Such practical coupled hydrodynamical and morphodynamical problems are not trivial to simulate since the geometry can be complex and the topography irregular. It should be pointed out that other mathematical models for morphodynamical systems have also been studied in [31, 23, 5] among others. In these systems, the shallow water equations have been coupled to an Exner-type equation for the bed-load without accounting for suspended sediments as it is shown in the current study.

The main concern of the sediment transport (or morphodynamics) is to determine the evolution of bed levels for hydrodynamic systems such as rivers, estuaries, bays and other nearshore regions where water flows interact with the bed geometry. Example of applications include among others, beach profile changes due to severe wave climates, seabed response to dredging procedures or imposed structures, and harbour siltation. The ability to design numerical methods able to predict the morphodynamics evolution of the coastal seabed has a clear mathematical and engineering relevances. In practice, morphodynamics involve coupling between a hydrodynamics model, which provides a description of the flow field leading to a specification of local sediment transport rates, and an equation for bed level change which expresses the conservative balance of sediment volume and its continual redistribution with time. Nowadays, much effort has been devoted to develop numerical schemes for morphodynamics models able to resolve all hydrodynamics and morphodynamics scales. In the current study, a class of finite volume methods is proposed for numerical simulation of transient flows involving erosion and deposition of sediments. The method consists of a predictor stage where the numerical fluxes are constructed and a corrector stage to recover the conservation equations. The sign matrix of the Jacobian matrix is used in the reconstruction of the numerical fluxes. Most of these techniques have been recently investigated in [5, 4] for solving morphodynmics models without accounting for sediment transport, erosion and deposition effects. The current study presents an extension of this method to transient flows involving erosion and deposition of sediments. A detailed formulation of the sign matrix and the numerical fluxes is presented using unstructured grids. It is well-known that unstructured grids can be highly advantageous based on their ability to provide local mesh refinement near important bathymetric features and structures. As a consequence, the ability to provide local mesh refinement where it is needed leads to improve accuracy for a given computational

cost as compared to methods that use fixed structured meshes. The proposed method also satisfies the property of well-balancing flux-gradient and source-term in the system. In the computations presented in the current study we have used the concentration of sediments as a monitoring function for mesh refinements. Results presented in this paper demonstrate high resolution of the proposed method and confirm its capability to provide accurate and efficient simulations for sediment transport by water flows including erosion and deposition effects in complex topography using unstructured grids. We should emphasize that higher order methods have also been used to solve nonconservative hyperbolic systems, see for example [11, 21]. However, no mesh adaptation has been carried out in these references.

This paper is organized as follows. In section 2 we briefly present the governing equations for coupled models of suspended sediment and bed-load transport in two-dimensional shallow water flows. The finite volume method is formulated in section 3. This section includes both the discretization of gradient fluxes and treatment of source terms. We also discuss a mesh adaptation for the this class of sediment transport problems. Section 4 contains numerical results and examples. Concluding remarks are summarized in section 5.

2 Governing sediment transport equations

In general, the sediment transport model consists of three parts: hydraulic variables describing the motion of water, a concentration variable describing the dispersion of suspended sediments, and a morphodynamics variable which describes the deformation of the bed-load. In the present work we assume that the flow is almost horizontal, the vertical component of the acceleration is vanishingly small, the pressure is taken to be hydrostatic, the free-surface gravity waves are long with respect to the mean flow depth and wave amplitude, and the water-species mixture is vertically homogeneous and non-reactive. The governing equations are obtained by balancing the net inflow of mass, momentum and species through boundaries of a control volume during an infinitesimal time interval while accounting for the accumulation of mass, resultant forces and species within the control volume, compare for example [1, 36] among others. Thus, the equations for mass conservation and momentum flux balance are given by

$$\begin{aligned}
\frac{\partial h}{\partial t}+\frac{\partial (hu)}{\partial x}+\frac{\partial (hv)}{\partial y} &= \frac{E-D}{1-p},\\
\frac{\partial (hu)}{\partial t}+\frac{\partial}{\partial x}\left(hu^2+\frac{1}{2}gh^2\right)+\frac{\partial}{\partial y}\left(huv\right) &= gh\left(-\frac{\partial Z}{\partial x}-S_f^x\right)-\frac{(\rho_s-\rho_w)}{2\rho}gh^2\frac{\partial c}{\partial x}\\
&\quad -\frac{(\rho_0-\rho)(E-D)}{\rho(1-p)}u,\\
\frac{\partial (hv)}{\partial t}+\frac{\partial}{\partial x}\left(huv\right)+\frac{\partial}{\partial y}\left(hv^2+\frac{1}{2}gh^2\right) &= gh\left(-\frac{\partial Z}{\partial y}-S_f^y\right)-\frac{(\rho_s-\rho_w)}{2\rho}gh^2\frac{\partial c}{\partial y}\\
&\quad -\frac{(\rho_0-\rho)(E-D)}{\rho(1-p)}v,
\end{aligned} \tag{1}$$

where t is the time variable, $\mathbf{x}=(x,y)^T$ the space coordinates, $\mathbf{u}=(u,v)^T$ the depth-averaged water velocity, h the water depth, Z the bottom topography, g the gravitational acceleration, p the porosity, ρ_w the water density, ρ_s the sediment density, c is the depth-averaged concentration of the suspended sediment, E and D represent the entrainment and deposition terms in upward and downward directions, respectively. In (1), ρ and ρ_0 are respectively, the density of the water-sediment mixture and the density of the saturated bed defined by

$$\rho=\rho_w(1-c)+\rho_s c, \qquad \rho_0=\rho_w p+\rho_s(1-p). \tag{2}$$

The friction slopes S_f^x and S_f^y are defined, using the Manning roughness coefficient n_b, as

$$S_f^x = \frac{n_b^2}{h^{4/3}} u\sqrt{u^2+v^2}, \qquad S_f^y = \frac{n_b^2}{h^{4/3}} v\sqrt{u^2+v^2}. \tag{3}$$

The equation for mass conservation of species is modeled by

$$\frac{\partial (hc)}{\partial t} + \frac{\partial}{\partial x}(huc) + \frac{\partial}{\partial y}(hvc) = E - D. \tag{4}$$

Note that an evolution equation for the density can also be obtained by substituting the concentration, $c = (\rho - \rho_w)/(\rho_s - \rho_w)$ from the relation (2), into the equation (4). It is evident that the density of the water-sediment mixture $\rho = \rho_w$ only if the concentration vanishes. To determine the entrainment and deposition terms in the above equations we assume a non-cohesive sediment and we use empirical relations reported in [14]. Thus,

$$D = w(1 - C_a)^m C_a, \tag{5}$$

where w is the settling velocity of a single particle in tranquil water

$$\omega = \frac{\sqrt{(36\nu/d)^2 + 7.5\rho_s g d} - 36\nu/d}{2.8}, \tag{6}$$

with ν is the kinematic viscosity of the water, d the averaged diameter of the sediment particle, m an exponent indicating the effects of hindered settling due to high sediment concentrations and it is set to $m = 2$ in our simulations, C_a the near-bed volumetric sediment concentration, $C_a = \alpha_c c$, where α_c is a coefficient larger than unity. To ensure that the near-bed concentration does not exceed $(1 - p)$, the coefficient α_c is computed by [13]

$$\alpha_c = \min\left(2, \frac{1-p}{c}\right).$$

For the entrainment of a cohesive material, the following relation is used

$$E = \begin{cases} \varphi \dfrac{\theta - \theta_c}{h}\sqrt{u^2+v^2}\, d^{-0.2}, & \text{if } \theta \geq \theta_c, \\ 0, & \text{otherwise,} \end{cases} \tag{7}$$

where φ is a coefficient to control the erosion forces, θ_c is a critical value of Shields parameter for the initiation of the sediment motion and θ is the Shields coefficient defined by

$$\theta = \frac{u_*^2}{sgd}, \tag{8}$$

with u_* is the friction velocity defined using the Darcy-Weisbach friction factor f as

$$u_*^2 = \sqrt{\frac{f}{8}}\sqrt{u^2+v^2}.$$

In (8), s is the submerged specific gravity of sediment given by

$$s = \frac{\rho_s}{\rho_w} - 1.$$

In this paper we are interested in sediment transport models over movable beds. There are different models for describing the movement of beds in shallow water flows and due to its complex nature only few theoretical models exist which use idealized and simplified assumptions. Most of the sediment models, which are used in practice, are empirical or semi-empirical and usually only work in particular

context and for this reason there is not yet a universally accepted theory of sediment transport, see for instance [36]. However, we can in general describe the total sediment transport through two processes. The sediment can move in a layer close to the bottom topography which is known as bed load and is characterized by a rolling and sliding movement, or the flow can cause the sediment to separate completely from the bottom in which case it is referred to as suspended load and in this case the sediment is transported as a concentration of the water column and will later be deposited in the bottom. In this work we shall consider total transport. We assume that the time scales we are interested in are much larger than the time scales required for the suspended sediments to deposit in the bottom. The author in [32] states that one can make this simplification when dealing with large distances and times. There is an interesting area of application of this problem, for example in the design of waterways or in the study of the capacity of a dam. Thus, to update the bedload, we consider the Exner equation (known by Grass formula) proposed in [19]

$$\frac{\partial Z}{\partial t} + \frac{A_s}{1-p}\frac{\partial}{\partial x}\big(u(u^2+v^2)\big) + \frac{A_s}{1-p}\frac{\partial}{\partial y}\big(v(u^2+v^2)\big) = -\frac{E-D}{1-p}, \tag{9}$$

where A_s is a coefficient usually obtained from experiments taking into account the grain diameter and the density of the sediments. In practice, the values of the coefficient A_s are taken between 0 and 1 depending on the interaction between the sediment transport and the water flow. Note that most of existing formulations for suspended sediment transport models are empirical to differing extents and have been derived from experiments and measured data. For more discussions on the mathematical and physical aspects of the considered suspended sediment equations we refer the reader to [12, 33] among others. It should be pointed out that in contrast to the equations discussed in these references, the governing equations in the current work account for movable beds using an Exner-type equation for the bed-load. Note that for clear water we assume that neither erosion nor deposition is taken place in the considered system (*i.e.* $E - D = 0$ in the above equations).

For simplicity in the presentation, let us rewrite the equations (1), (4) and (9) in the following vector form

$$\frac{\partial \mathbf{W}}{\partial t} + \frac{\partial \mathbf{F}(\mathbf{W})}{\partial x} + \frac{\partial \mathbf{G}(\mathbf{W})}{\partial y} = \mathbf{S}(\mathbf{W}) + \mathbf{Q}(\mathbf{W}), \tag{10}$$

where $\mathbf{W}$ is the vector of conserved variables, $\mathbf{F}$ and $\mathbf{G}$ are the physical fluxes in x- and y-direction, $\mathbf{S}$ and $\mathbf{Q}$ are the source terms. These variables are defined as

$$\mathbf{W} = \begin{pmatrix} h \\ hu \\ hv \\ hc \\ Z \end{pmatrix}, \quad \mathbf{F}(\mathbf{W}) = \begin{pmatrix} hu \\ hu^2 + \frac{1}{2}gh^2 \\ huv \\ huc \\ \frac{A_s}{1-p}u(u^2+v^2) \end{pmatrix}, \quad \mathbf{G}(\mathbf{W}) = \begin{pmatrix} hv \\ huv \\ hv^2 + \frac{1}{2}gh^2 \\ hvc \\ \frac{A_s}{1-p}v(u^2+v^2) \end{pmatrix},$$

$$\mathbf{S}(\mathbf{W}) = \begin{pmatrix} 0 \\ -gh\frac{\partial Z}{\partial x} - \frac{(\rho_s-\rho_w)}{2\rho}gh^2\frac{\partial c}{\partial x} \\ -gh\frac{\partial Z}{\partial y} - \frac{(\rho_s-\rho_w)}{2\rho}gh^2\frac{\partial c}{\partial y} \\ 0 \\ 0 \end{pmatrix}, \quad \mathbf{Q}(\mathbf{W}) = \begin{pmatrix} \frac{E-D}{1-p} \\ -ghS_f^x - \frac{(\rho_0-\rho)(E-D)}{\rho(1-p)}u \\ -ghS_f^y - \frac{(\rho_0-\rho)(E-D)}{\rho(1-p)}v \\ E-D \\ -\frac{E-D}{1-p} \end{pmatrix}.$$

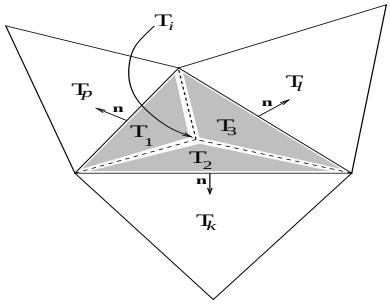

Figure 1: A generic control volume $\mathcal{T}_i$ and notations.

It is worth emphasizing that, using the Exner equation (9) to model the bed-load transport, the non-homogenuous terms in the right-hand side in (10) are not standard source terms but nonconservative products, since they include derivatives of two of the variables. The presence of these terms in the sediment transport system can cause severe difficulties in their numerical approximations, see for instance [15]. In principle, the nonhomegenuous term in these equations can be viewed as a source term and/or a nonconservative term. In the approach presented in this study these terms are considered and discretized as source terms.

3 Unstructured finite volume method

The governing sediment transport equations (10) are formulated in Cartesian coordinates and will be discretized on the unstructured grids by the finite volume method. The unstructured grids are polygons and the number of edges of the grids is not limited in theory, but only triangular grids are considered in the current study. Hence, we divide the time interval into sub-intervals $[t_n, t_{n+1}]$ with stepsize Δt and discretize the spatial domain in conforming triangular elements $\mathcal{T}_i$. Each triangle represents a control volume and the variables are located at the geometric centres of the cells. Hence, using the control volume depicted in Figure 1, a finite volume discretization of (10) yields

$$\begin{aligned} \mathbf{W}_i^{n+1} &= \mathbf{W}_i^n - \frac{\Delta t}{|\mathcal{T}_i|} \sum_{j \in N(i)} \int_{\Gamma_{ij}} \mathcal{F}(\mathbf{W}^n; \mathbf{n})\, d\sigma + \\ & \frac{\Delta t}{|\mathcal{T}_i|} \int_{\mathcal{T}_i} \mathbf{S}(\mathbf{W}^n)\, dV + \frac{\Delta t}{|\mathcal{T}_i|} \int_{\mathcal{T}_i} \mathbf{Q}(\mathbf{W}^n)\, dV, \end{aligned} \tag{11}$$

where $N(i)$ is the set of neighboring triangles of the cell $\mathcal{T}_i$, $\mathbf{W}_i^n$ is an averaged value of the solution $\mathbf{W}$ in the cell $\mathcal{T}_i$ at time t_n,

$$\mathbf{W}_i = \frac{1}{|\mathcal{T}_i|} \int_{\mathcal{T}_i} \mathbf{W}\, dV,$$

where $|\mathcal{T}_i|$ denotes the area of $\mathcal{T}_i$. Here, Γ_{ij} is the interface between the two control volumes $\mathcal{T}_i$ and $\mathcal{T}_j$, $\mathbf{n} = (n_x, n_y)^T$ denotes the unit outward normal to Γ_{ij}, and

$$\mathcal{F}(\mathbf{W}; \mathbf{n}) = \mathbf{F}(\mathbf{W}) n_x + \mathbf{G}(\mathbf{W}) n_y.$$

To deal with the source terms $\mathbf{Q}$, a standard splitting procedure (see for instance [9]) is employed for the discrete system (11) as

$$\begin{aligned} \mathbf{W}_i^* &= \mathbf{W}_i^n - \frac{\Delta t}{|\mathcal{T}_i|} \sum_{j \in N(i)} \int_{\Gamma_{ij}} \mathcal{F}(\mathbf{W}^n; \mathbf{n})\, d\sigma + \frac{\Delta t}{|\mathcal{T}_i|} \int_{\mathcal{T}_i} \mathbf{S}(\mathbf{W}^n)\, dV, \\ \mathbf{W}_i^{n+1} &= \mathbf{W}_i^* + \frac{\Delta t}{|\mathcal{T}_i|} \int_{\mathcal{T}_i} \mathbf{Q}(\mathbf{W}^*)\, dV. \end{aligned} \tag{12}$$

Note that the time splitting (12) is only first-order accurate. A second-order splitting for the system (11) can be derived analogously using the Strang method [34]. The finite volume discretization (12) is complete once the gradient fluxes $\mathcal{F}(\mathbf{W};\mathbf{n})$ and a discretization of source terms $\mathbf{Q}(\mathbf{W}^n)$ and $\mathbf{S}(\mathbf{W}^n)$ are well defined.

3.1 Discretization of the gradient fluxes

Let us consider the system (10) without the source term $\mathbf{Q}(\mathbf{W})$ given by

$$\frac{\partial \mathbf{W}}{\partial t} + \frac{\partial \mathbf{F}(\mathbf{W})}{\partial x} + \frac{\partial \mathbf{G}(\mathbf{W})}{\partial y} = \mathbf{S}(\mathbf{W}). \tag{13}$$

Applied to the system (13), the finite volume discretization over the control volume $\mathcal{T}_i$ yields

$$\begin{aligned}
\frac{\partial}{\partial t}\int_{\mathcal{T}_i} h\, dV + \oint_{\mathcal{S}_i} (hun_x + hvn_y)\, d\sigma &= 0,\\
\frac{\partial}{\partial t}\int_{\mathcal{T}_i} hu\, dV + \oint_{\mathcal{S}_i} \left(\left(hu^2 + \frac{1}{2}gh^2\right)n_x + huvn_y\right) d\sigma &= -gh\left(\mathcal{T}_i\right)\oint_{\mathcal{S}_i} Zn_x\, d\sigma - \\
&\quad \frac{(\rho_s-\rho_w)}{2\rho}gh^2\left(\mathcal{T}_i\right)\oint_{\mathcal{S}_i} cn_x\, d\sigma,\\
\frac{\partial}{\partial t}\int_{\mathcal{T}_i} hv\, dV + \oint_{\mathcal{S}_i} \left(huvn_x + \left(hv^2 + \frac{1}{2}gh^2\right)n_y\right) d\sigma &= -gh\left(\mathcal{T}_i\right)\oint_{S_i} Zn_y\, d\sigma - \\
&\quad \frac{(\rho_s-\rho_w)}{2\rho}gh^2\left(\mathcal{T}_i\right)\oint_{\mathcal{S}_i} cn_y\, d\sigma,\\
\frac{\partial}{\partial t}\int_{\mathcal{T}_i} hc\, dV + \oint_{\mathcal{S}_i} (hucn_x + hvcn_y)\, d\sigma &= 0,\\
\frac{\partial}{\partial t}\int_{\mathcal{T}_i} Z\, dV + \frac{A_s}{1-p}\oint_{\mathcal{S}_i} \left(u\left(u^2+v^2\right)n_x + v(u^2+v^2)n_y\right) d\sigma &= 0,
\end{aligned}$$

where $\mathcal{S}_i$ is the surface surrounding the control volume $\mathcal{T}_i$ and $h\left(\mathcal{T}_i\right)$ represents an approximation of h in $\mathcal{T}_i$, see [2] for similar techniques applied to compressible flows. Using the expressions of the normal velocity $u_\eta = un_x + vn_y$ and tangential velocity $u_\tau = -un_y + vn_x$, the above equations can be reformulated as

$$\begin{aligned}
\frac{\partial}{\partial t}\int_{\mathcal{T}_i} h\, dV + \oint_{\mathcal{S}_i} hu_\eta\, d\sigma &= 0,\\
\frac{\partial}{\partial t}\int_{\mathcal{T}_i} hu\, dV + \oint_{\mathcal{S}_i} \left(huu_\eta + \frac{1}{2}gh^2n_x\right) d\sigma &= -gh\left(\mathcal{T}_i\right)\oint_{S_i} Zn_x\, d\sigma - \\
&\quad \frac{(\rho_s-\rho_w)}{2\rho}gh^2\left(\mathcal{T}_i\right)\oint_{\mathcal{S}_i} cn_x\, d\sigma,\\
\frac{\partial}{\partial t}\int_{\mathcal{T}_i} hv\, dV + \oint_{\mathcal{S}_i} \left(hvu_\eta + \frac{1}{2}gh^2n_y\right) d\sigma &= -gh\left(\mathcal{T}_i\right)\oint_{S_i} Zn_y\, d\sigma - \\
&\quad \frac{(\rho_s-\rho_w)}{2\rho}gh^2\left(\mathcal{T}_i\right)\oint_{\mathcal{S}_i} cn_y\, d\sigma,\\
\frac{\partial}{\partial t}\int_{\mathcal{T}_i} hc\, dV + \oint_{\mathcal{S}_i} hu_\eta c d\sigma &= 0,\\
\frac{\partial}{\partial t}\int_{\mathcal{T}_i} Z\, dV + \frac{A_s}{1-p}\oint_{\mathcal{S}_i} \left(u^2+v^2\right)u_\eta\, d\sigma &= 0.
\end{aligned} \tag{14}$$

In order to simplify the system (14), in a first operation we multiply the second equation by n_x and in the second operation we multiply the third equation by n_y, then the obtained equation from the first

operation is added to the one obtained from the second operation. In the second step we subtract the obtained equation from the second operation from the one obtained from the first operation. The result of these operations is

$$\begin{aligned}
\frac{\partial}{\partial t}\int_{\mathcal{T}_i} h\, dV + \oint_{\mathcal{S}_i} hu_\eta\, d\sigma &= 0,\\
\frac{\partial}{\partial t}\int_{\mathcal{T}_i} hu_\eta\, dV + \oint_{\mathcal{S}_i}\left(hu_\eta u_\eta + \frac{1}{2}gh^2\right) d\sigma &= -gh\left(\mathcal{T}_i\right)\oint_{S_i} Z\, d\sigma - \\
&\quad \frac{(\rho_s-\rho_w)}{2\rho}gh^2\left(\mathcal{T}_i\right)\oint_{\mathcal{S}_i} c\, d\sigma,\\
\frac{\partial}{\partial t}\int_{\mathcal{T}_i} hu_\tau\, dV + \oint_{\mathcal{S}_i} hu_\tau u_\eta\, d\sigma &= 0,\\
\frac{\partial}{\partial t}\int_{\mathcal{T}_i} hc\, dV + \oint_{\mathcal{S}_i} hu_\eta c d\sigma &= 0,\\
\frac{\partial}{\partial t}\int_{\mathcal{T}_i} Z\, dV + \frac{A_s}{1-p}\oint_{\mathcal{S}_i}\left(u^2+v^2\right)u_\eta\, d\sigma &= 0,
\end{aligned} \tag{15}$$

which can be reformulated in a differential form as

$$\begin{aligned}
\frac{\partial h}{\partial t} + \frac{\partial\left(hu_\eta\right)}{\partial \eta} &= 0,\\
\frac{\partial\left(hu_\eta\right)}{\partial t} + \frac{\partial}{\partial\eta}\left(hu_\eta^2 + \frac{1}{2}gh^2\right) &= -gh\frac{\partial Z}{\partial\eta} - \frac{(\rho_s-\rho_w)}{2\rho}gh^2\frac{\partial c}{\partial\eta},\\
\frac{\partial\left(hu_\tau\right)}{\partial t} + \frac{\partial}{\partial\eta}\left(hu_\eta u_\tau\right) &= 0,\\
\frac{\partial\left(hc\right)}{\partial t} + \frac{\partial}{\partial\eta}\left(hu_\eta c\right) &= 0,\\
\frac{\partial Z}{\partial t} + \frac{\partial}{\partial\eta}\left(\frac{A_s}{1-p}u_\eta(u_\eta^2+u_\tau^2)\right) &= 0.
\end{aligned} \tag{16}$$

An equivalent system of (16) can also be rewritten in a vector form as

$$\frac{\partial \mathbf{U}}{\partial t} + \mathbf{A}_\eta(\mathbf{U})\frac{\partial \mathbf{U}}{\partial \eta} = \mathbf{0}. \tag{17}$$

where

$$\mathbf{U} = \begin{pmatrix} h \\ hu_\eta \\ hu_\tau \\ hc \\ Z \end{pmatrix},$$

$$\mathbf{A}_\eta(\mathbf{U}) = \begin{pmatrix}
0 & 1 & 0 & 0 & 0\\
gh - u_\eta^2 - \dfrac{(\rho_s-\rho_w)}{2\rho}ghc & 2u_\eta & 0 & \dfrac{(\rho_s-\rho_w)}{2\rho}gh & gh\\
-u_\eta u_\tau & u_\tau & u_\eta & 0 & 0\\
-u_\eta c & c & 0 & u_\eta & 0\\
-\dfrac{A_s}{1-p}\dfrac{3u_\eta(u_\eta^2+u_\tau^2)}{h} & \dfrac{A_s}{1-p}\dfrac{3\,u_\eta^2+u_\tau^2}{h} & \dfrac{A_s}{1-p}\dfrac{2u_\eta\,u_\tau}{h} & 0 & 0
\end{pmatrix}.$$

One of the advantages in considering the projected system (17) is that no discretization of source terms is required. Thus, in the predictor stage, we use the projected system (17) to compute the averaged states as

$$\mathbf{U}_{ij}^n = \frac{1}{2}\left(\mathbf{U}_i^n + \mathbf{U}_j^n\right) - \frac{1}{2}\operatorname{sgn}\Big[\mathbf{A}_\eta\left(\overline{\mathbf{U}}\right)\Big]\left(\mathbf{U}_j^n - \mathbf{U}_i^n\right), \tag{18}$$

where the sign matrix of the Jacobian is defined as

$$\operatorname{sgn}\Big[\nabla\mathbf{F}_\eta\left(\overline{\mathbf{U}}\right)\Big] = \mathcal{R}(\overline{\mathbf{U}})\operatorname{sgn}\Big[\Lambda(\overline{\mathbf{U}})\Big]\mathcal{R}^{-1}(\overline{\mathbf{U}}),$$

with $\Lambda(\overline{\mathbf{U}})$ is the diagonal matrix of eigenvalues, and $\mathcal{R}(\overline{\mathbf{U}})$ is the right eigenvector matrix. These matrices can be explicitly expressed using the associated eigenvalues of $\mathbf{A}_\eta(\mathbf{U})$ in (17). For convenience of the reader, the matrices $\mathcal{R}(\overline{\mathbf{U}})$ and $\mathcal{R}^{-1}(\overline{\mathbf{U}})$ are formulated in the Appendix. Here, $\overline{\mathbf{U}}$ is the intermediate averaged state given by

$$\overline{\mathbf{U}} = \begin{pmatrix} \dfrac{h_i+h_j}{2} \\ \dfrac{h_i+h_j}{2}\left(\dfrac{u_i\sqrt{h_i}+u_j\sqrt{h_j}}{\sqrt{h_i}+\sqrt{h_j}}\eta_x + \dfrac{v_i\sqrt{h_i}+v_j\sqrt{h_j}}{\sqrt{h_i}+\sqrt{h_j}}\eta_y\right) \\ \dfrac{h_i+h_j}{2}\left(-\dfrac{u_i\sqrt{h_i}+u_j\sqrt{h_j}}{\sqrt{h_i}+\sqrt{h_j}}\eta_y + \dfrac{v_i\sqrt{h_i}+v_j\sqrt{h_j}}{\sqrt{h_i}+\sqrt{h_j}}\eta_x\right) \\ \dfrac{h_i+h_j}{2}\left(\dfrac{c_i\sqrt{h_i}+c_j\sqrt{h_j}}{\sqrt{h_i}+\sqrt{h_j}}\right) \\ \dfrac{Z_i+Z_j}{2} \end{pmatrix}. \tag{19}$$

Once the states $\mathbf{U}_{ij}^n$ are calculated in the predictor stage (18), the states $\mathbf{W}_{ij}^n$ are recovered by using the transformations $v = (u_\tau, u_\eta)\cdot\eta$ and $u = (u_\tau, u_\eta)\cdot\tau$. Thus, applied to the system (13), the proposed finite volume method consists of a predictor stage and a corrector stage and can be formulated as:

$$\begin{aligned} \mathbf{U}_{ij}^n &= \frac{1}{2}\left(\mathbf{U}_i^n + \mathbf{U}_j^n\right) - \frac{1}{2}\operatorname{sgn}\Big[\mathbf{A}_\eta\left(\overline{\mathbf{U}}\right)\Big]\left(\mathbf{U}_j^n - \mathbf{U}_i^n\right), \\ \mathbf{W}_i^{n+1} &= \mathbf{W}_i^n - \frac{\Delta t}{|\mathcal{T}_i|}\sum_{j\in N(i)}\mathcal{F}\left(\mathbf{W}_{ij}^n;\eta_{ij}\right)|\Gamma_{ij}| + \Delta t\mathbf{S}_i^n. \end{aligned} \tag{20}$$

It is worth remarking that for sonic shocks and transonic rarefactions the well-established *entropy fix* developed in [22] is used. Next we discuss the treatment of source terms $\mathbf{S}_i^n$ in the proposed finite volume scheme and also the extension of the scheme to a second-order accuracy. An adaptive procedure is also described in this section.

3.2 Treatment of the source term

The treatment of the source terms in the shallow water equations presents a challenge in many numerical methods, compare [4] among others. In our scheme, the source term approximation $\mathbf{S}_i^n$ in the corrector stage is reconstructed such that the still-water equilibrium (C-property) [7] is satisfied. Here, a numerical scheme is said to satisfy the C-property for the equations (10) if the condition

$$E - D = 0, \qquad u = 0, \qquad Z = \bar{Z}(x), \qquad h + Z = H, \qquad \rho = C, \tag{21}$$

holds for stationary flows at rest. In (21), H and C are nonnegative constants. Therefore, the treatment of source terms in (20) is reconstructed such that the condition (21) is preserved at the

discretized level. Remark that the last condition in (21) means that at the equilibrium the sediment medium is assumed to be saturated. Furthermore, from the density equation (2), a constant density is equivalent to a constant concentration c. Hence, $\mathbf{S}_i^n$ should be a consistent discretization of the source term in (13) defined as

$$\mathbf{S}_i^n = \begin{pmatrix} 0 \\ -g\bar{h}_{xi}^n \sum\limits_{j\in N(i)} Z_{ij}^n n_{xij} \left|\Gamma_{ij}\right| - \dfrac{(\rho_s-\rho_w)}{2\rho} g \left(\bar{h}_{xi}^n\right)^2 \sum\limits_{j\in N(i)} c_{ij}^n n_{xij} \left|\Gamma_{ij}\right| \\ -g\bar{h}_{yi}^n \sum\limits_{j\in N(i)} Z_{ij}^n n_{yij} \left|\Gamma_{ij}\right| - \dfrac{(\rho_s-\rho_w)}{2\rho} g \left(\bar{h}_{yi}^n\right)^2 \sum\limits_{j\in N(i)} c_{ij}^n n_{yij} \left|\Gamma_{ij}\right| \\ 0 \\ 0 \end{pmatrix}. \tag{22}$$

The approximations $\bar{h}_{xi}^n$ and $\bar{h}_{yi}^n$ are reconstructed using a technique recently developed in [4] for the proposed finite volume method to satisfy the well-known C-property in the standard shallow water flow over fixed beds. In this section we briefly describe the formulation of this procedure and more details can be found in [4]. Hence, at the stationary state, the numerical flux in the corrector stage yields

$$\sum_{j\in N(i)} \mathcal{F}\left(\mathbf{W}_{ij}^n; \mathbf{n}_{ij}\right) = \begin{pmatrix} 0 \\ -g\displaystyle\int_{\mathcal{T}_i} h\frac{\partial Z}{\partial x}\, dV \\ -g\displaystyle\int_{\mathcal{T}_i} h\frac{\partial Z}{\partial y}\, dV \\ 0 \\ 0 \end{pmatrix},$$

which is equivalent to

$$\begin{pmatrix} 0 \\ \displaystyle\sum_{j\in N(i)} \frac{1}{2} g \left(h_{ij}^n\right)^2 N_{xij} \\ \displaystyle\sum_{j\in N(i)} \frac{1}{2} g \left(h_{ij}^n\right)^2 N_{yij} \\ 0 \\ 0 \end{pmatrix} = \begin{pmatrix} 0 \\ -g\displaystyle\int_{\mathcal{T}_i} h\frac{\partial Z}{\partial x}\, dV \\ -g\displaystyle\int_{\mathcal{T}_i} h\frac{\partial Z}{\partial y}\, dV \\ 0 \\ 0 \end{pmatrix}. \tag{23}$$

where $N_{xij} = n_{xij}\left|\Gamma_{ij}\right|$ and $N_{yij} = n_{yij}\left|\Gamma_{ij}\right|$. Next, to approximate the source terms we proceed as follows. First we decompose the triangle $\mathcal{T}_i$ into three sub-triangles as depicted in Figure 1. Then, the source term is approximated as

$$\int_{\mathcal{T}_i} h\frac{\partial Z}{\partial x}\, dV = \int_{\mathcal{T}_1} h\frac{\partial Z}{\partial x}\, dV + \int_{\mathcal{T}_2} h\frac{\partial Z}{\partial x}\, dV + \int_{\mathcal{T}_3} h\frac{\partial Z}{\partial x}\, dV, \tag{24}$$

where

$$\int_{\mathcal{T}_1} h\frac{\partial Z}{\partial x}\, dV = h_1 \int_{\mathcal{T}_1} \frac{\partial Z}{\partial x}\, dV,$$

with h_1 is an average value of h on the sub-triangle $\mathcal{T}_1$. Hence,

$$\begin{aligned}\int_{\mathcal{T}_1} h\frac{\partial Z}{\partial x}\,dV &= h_1 \sum_{j\in N(1)} \int_{\Gamma_{1j}} Z n_x\,d\sigma,\\ &= h_1 \sum_{j\in N(1)} Z_{1j}\,N_{x1j},\\ &= h_1 \sum_{j\in N(1)} \frac{Z_1+Z_j}{2}\,N_{x1j}. \end{aligned} \tag{25}$$

Again, using the stationary flow condition $h_1 + Z_1 = H$ and $h_j + Z_j = H$, one gets

$$h_1 + Z_1 + h_j + Z_j = 2H \qquad \text{and} \qquad \frac{Z_1+Z_j}{2} = H - \frac{h_1+h_j}{2}.$$

Thus, (25) gives

$$\int_{\mathcal{T}_1} h\frac{\partial Z}{\partial x}\,dV = h_1 \sum_{j\in N(1)} \left(H - \frac{h_1+h_j}{2}\right) N_{x1j}.$$

Using the fact that $\displaystyle\sum_{j\in N(1)} N_{x1j} = 0$,

$$\begin{aligned}\int_{\mathcal{T}_1} h\frac{\partial Z}{\partial x}\,dV &= -\frac{h_1}{2} \sum_{j\in N(1)} h_j\,N_{x1j},\\ &= -\frac{h_1}{2}\left(h_p N_{x1p} + h_2 N_{x12} + h_3 N_{x13}\right).\end{aligned}$$

A similar procedure leads to the following approximations of the other terms in (24)

$$\begin{aligned}\int_{\mathcal{T}_2} h\frac{\partial Z}{\partial x}\,dV &= -\frac{h_2}{2}\left(h_k N_{x2k} + h_1 N_{x21} + h_3 N_{x23}\right),\\ \int_{\mathcal{T}_3} h\frac{\partial Z}{\partial x}\,dV &= -\frac{h_3}{2}\left(h_l N_{x3l} + h_1 N_{x31} + h_2 N_{x32}\right).\end{aligned}$$

Notice that h_p, h_k and h_l are the average values of h respectively, on the triangle $\mathcal{T}_p$, $\mathcal{T}_k$ and $\mathcal{T}_l$, see Figure 1. Summing up, the discretization (24) gives

$$\int_{\mathcal{T}_i} h\frac{\partial Z}{\partial x}\,dV = -\frac{h_1}{2}h_p N_{x1p} - \frac{h_2}{2}h_k N_{x2k} - \frac{h_3}{2}h_l N_{x3l}.$$

For this reconstruction, the source terms in (23) result in

$$\begin{aligned}\sum_{j\in N(i)} \left(h_{ij}^n\right)^2 N_{xij} &= h_1\left(h_p N_{x1p}\right) + h_2\left(h_k N_{x2k}\right) + h_3\left(h_l N_{x3l}\right),\\ \sum_{j\in N(i)} \left(h_{ij}^n\right)^2 N_{yij} &= h_1\left(h_p N_{y1p}\right) + h_2\left(h_k N_{y2k}\right) + h_3\left(h_l N_{y3l}\right).\end{aligned} \tag{26}$$

Here, (26) forms a linear system of two equations for the three unknowns h_1, h_2 and h_3. To complete the system we add the natural conservation equation

$$h_1 + h_2 + h_3 = 3h_i.$$

Analogously, the bottom values Z_j^n, $j = 1, 2, 3$ are reconstructed in each sub-triangle of $\mathcal{T}_i$ as

$$Z_j^n + h_j^n = Z_i^n + h_i^n, \qquad j = 1, 2, 3.$$

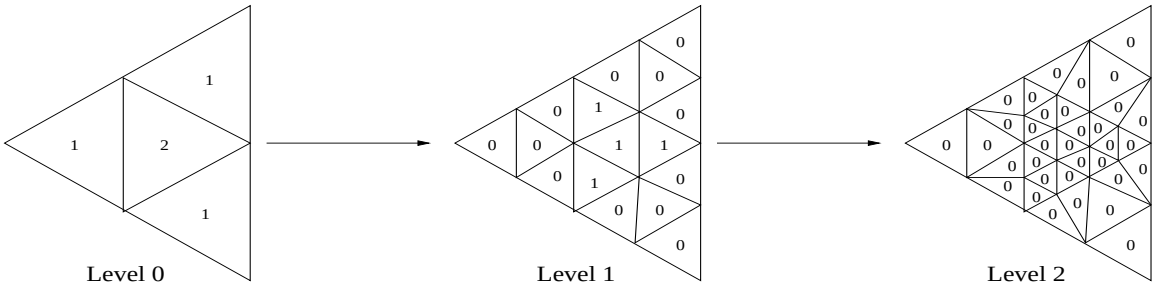

Figure 2: Illustration of a two-level refining for triangular elements. The numbers in the figure refer to the number of refinements to be performed for each sub-triangle.

Finally, the source terms in (24) are approximated as

$$\begin{aligned} h_1 \int_{\mathcal{T}_1} \frac{\partial Z}{\partial x}\, dV &= h_1 \left(\frac{Z_1 + Z_p}{2} N_{x1p} + \frac{Z_1 + Z_2}{2} N_{x12} + \frac{Z_1 + Z_3}{2} N_{x13} \right), \\ h_2 \int_{\mathcal{T}_1} \frac{\partial Z}{\partial x}\, dV &= h_2 \left(\frac{Z_2 + Z_k}{2} N_{x2k} + \frac{Z_2 + Z_1}{2} N_{x21} + \frac{Z_2 + Z_3}{2} N_{x23} \right), \\ h_3 \int_{\mathcal{T}_1} \frac{\partial Z}{\partial x}\, dV &= h_3 \left(\frac{Z_3 + Z_l}{2} N_{x3l} + \frac{Z_3 + Z_1}{2} N_{x31} + \frac{Z_3 + Z_2}{2} N_{x32} \right), \end{aligned} \tag{27}$$

with a similar equation for the other source terms in the y-direction. Numerical results reported in [4] have shown that the above reconstruction exactly preserves the C-property to the machine precision.

3.3 Adaptivity procedure

The mesh generation is based on the Delaunay triangulation, which uses a curvature-dependent generation strategy designed to produce smaller elements in regions of high curvature in the spatial domain. In order to improve the efficiency of the proposed finite volume method, we have performed a mesh adaptation to construct a nearly optimal mesh able to capture the small hydraulic features without relying on extremely fine grid in smooth regions far from hydraulic jumps and steep concentration gradients. In the present work, this goal is achieved by using an error indicator for the gradient of the sediment concentration. This indicator requires only information from solution values within a single element at a time and it is easily calculated. The adaptive procedure used here is based on multilevel refinement and unrefinement, it is aimed at constructing an adaptive mesh which dynamically follows the unsteady solution of the physical problem. This procedure has been used in [17] for adaptive finite volume solution of a combustion system and in [6] for pollutant transport by shallow water flows. The algorithm begins by selecting some criterion (here based on the gradient of the sediment concentration), which permits to make the refinement and unrefinement decisions. A list $\mathbf{T}$ of elements to be refined, their degree of refinement, and those to be unrefined is then established. This is accomplished by filling an integer array denoted for example by $\mathbb{I}$ for all triangles of the coarse mesh. At time $t = t^n$ and for a macro-element $\mathcal{T}_i$ we set $\mathbb{I}(\mathcal{T}_i) = m$ which means that the element $\mathcal{T}_i$ has to be divided into 4^m triangles. Thus, starting from a mesh level l, made of $N^{(l)}$ cells, the next mesh level contains $N^{(l+1)} = 4 \times N^{(l)}$ cells. Clearly, this process can be repeated as long as $l < m_{max}$ with m_{max} being the number of refinement levels. In order to obtain a mesh which is not too distorted, the algorithm decides to divide into two equal parts some additional edges. An illustration of the procedure is shown in Figure 2.

In our simulations, the mesh adaptation criterion is based on the normalized gradient of the sediment concentration and it is evaluated as

$$C^n_{\mathcal{T}_i} = \frac{\|\nabla\left(c(\mathcal{T}_i)\right)\|}{\max\limits_{\mathcal{T}_j} \|\nabla\left(c(\mathcal{T}_j)\right)\|}, \tag{28}$$

where $\|\nabla(c(\mathcal{T}_i))\|$ is the Euclidean norm of the gradient of the sediment concentration c on the triangle $\mathcal{T}_i$. The advantage of this normalization is that the criterion (28) is known to take its values in the interval $[0,1]$. Hence, an adaptation procedure can be performed as follows:

Given a sequence of three real numbers $\{r_m\}$ such that $0 = r_0 < r_1 < r_2 < r_3 = 1$. If a macro-element $\mathcal{T}_i$ satisfies the condition

$$r_m \leq C^n_{\mathcal{T}_i} \leq r_{m+1}, \qquad m = 0, 1, 2,$$

then the triangle $\mathcal{T}_i$ is divided into 4^m triangles. Note that the values of $\{r_1, r_2\}$ can be interpreted as tolerances to be set by the user resulting into a two-level refining. In our simulations presented in section 4 we have used a two-level and four-level refinements. It should be stressed that other adaptation criteria using the water free-surface or bed-load are also possible. Furthermore, to resolve the wetting/drying fronts in our finite volume scheme, we have adopted the same techniques proposed in [10]. Implementation details can be found in this reference and are omitted here.

3.4 Extension to second-order accuracy

Obviously, the discretization (20) is only first-order accurate. In order to develop a second-order finite volume scheme, we use a MUSCL method incorporating slope limiters in the spatial approximation and a two-step Runge-Kutta method for the time integration. The MUSCL discretization uses an approximation of the solution state $\mathbf{W}$ by linear interpolation at each cell interface Γ_{ij} as

$$\mathbf{W}_{ij} = \mathbf{W}_i + \frac{1}{2}\nabla\mathbf{W}_i \cdot \mathbf{d}_{ij}, \qquad \mathbf{W}_{ji} = \mathbf{W}_j - \frac{1}{2}\nabla\mathbf{W}_j \cdot \mathbf{d}_{ij}, \tag{29}$$

where $\mathbf{x}_i = (x_i, y_i)^T$ and $\mathbf{x}_j = (x_j, y_j)^T$ are respectively, the barycentric coordinates of cells $\mathcal{T}_i$ and $\mathcal{T}_j$, and $\mathbf{d}_{ij}$ is the distance between $\mathbf{x}_i$ and $\mathbf{x}_j$. Thus, the cell gradients are evaluated by minimizing the quadratic functional

$$\Psi_i(x, y) = \sum_{j \in M(i)} \left|\mathbf{W}_i + (x_j - x_i)x + (y_j - y_i)y - \mathbf{W}_j\right|^2, \tag{30}$$

where $M(i)$ is the set of indices of neighboring cells that have a common edge or vertex with the control volume $\mathcal{T}_i$. For instance, the cell gradients $\nabla\mathbf{W}_i = \left(\frac{\partial\mathbf{W}_i}{\partial x}, \frac{\partial\mathbf{W}_i}{\partial y}\right)^T$ in (29) are solutions of the linear system

$$\frac{\partial\Psi_i(x,y)}{\partial x} = 0, \qquad \frac{\partial\Psi_i(x,y)}{\partial y} = 0.$$

It is easy to verify that

$$\frac{\partial\mathbf{W}_i}{\partial x} = \frac{J_x I_{yy} - J_y I_{xy}}{I_{xx}I_{yy} - I_{xy}I_{yx}}, \qquad \frac{\partial\mathbf{W}_i}{\partial y} = \frac{J_y I_{xx} - J_x I_{yx}}{I_{xx}I_{yy} - I_{xy}I_{yx}}, \tag{31}$$

where

$$I_{xx} = \sum_{j \in M(i)} (x_j - x_i)^2, \quad I_{yy} = \sum_{j \in M(i)} (y_j - y_i)^2, \quad I_{xy} = I_{yx} = \sum_{j \in M(i)} (x_j - x_i)(y_j - y_i),$$

$$J_x = \sum_{j \in M(i)} (x_j - x_i)(\mathbf{W}_j - \mathbf{W}_i), \qquad J_y = \sum_{j \in M(i)} (y_j - y_i)(\mathbf{W}_j - \mathbf{W}_i).$$

In order to obtain a TVD scheme, we incorporate slope limiters to the reconstruction (29) using the MinMod limiter function. This is achieved by replacing the cell gradients in (31) by

$$\frac{\partial^{\lim}\mathbf{W}_i}{\partial x} = \frac{1}{2}\left(\min_{j \in M(i)} \operatorname{sgn}\left[\frac{\partial\mathbf{W}_j}{\partial x}\right] + \max_{j \in M(i)} \operatorname{sgn}\left[\frac{\partial\mathbf{W}_j}{\partial x}\right]\right) \min_{j \in M(i)} \left|\frac{\partial\mathbf{W}_j}{\partial x}\right|, \tag{32}$$

with a similar expression for $\frac{\partial^{\lim}\mathbf{W}_i}{\partial y}$. Note that other slope limiter functions from [22] can also be implemented in our finite volume method without major conceptual modifications. It should be pointed out that, in order to achieve a second-order accuracy in the proposed finite volume method, the state solutions $\mathbf{W}_{ij}$ and $\mathbf{W}_{ji}$ in the discretization of gradient fluxes and source terms should be replaced by the second-order reconstruction (29). Finally, to discretize the friction and erosion-deposition terms contained in the source term $\mathbf{Q}(\mathbf{W})$ in (10), we consider an operator splitting procedure. Thus, the system (10) is decomposed in two equations as

$$\begin{aligned} \frac{\partial \mathbf{W}}{\partial t} + Res(\mathbf{W}) &= \mathbf{S}(\mathbf{W}), \\ \frac{\partial \mathbf{W}}{\partial t} &= \mathbf{Q}(\mathbf{W}), \end{aligned} \tag{33}$$

where *Res* describes the convection terms in the momentum equation corresponding to the surface integral in (10) and it is approximated as the sum taken over all edges of each element in the computational mesh.

First, an explicit method is used to integrate the first equation in (33) leading to

$$\frac{\widetilde{\mathbf{W}} - \mathbf{W}^n}{\Delta t} + Res(\mathbf{W}^n) = \mathbf{S}(\mathbf{W}^n).$$

In the second step, the state solution $\widetilde{\mathbf{W}}$ is taken to be the initial condition when solving the second equation in (33).

The implementation of boundary conditions in the finite volume method is performed using similar techniques as those described in [25]. For the computational examples considered in this paper, boundary conditions are enforced on the corrector solution by computing fluxes at cell boundaries. On the predictor solution and the slopes of dependent variables, boundary conditions are enforced in boundary cells by setting the required variables to the corresponding values of the adjacent inner cells. When slopes are based on vertex values, the solution at boundary vertices is computed by interpolation from two neighboring centroids. When slopes are based on centroid values, the three points used to estimate the slopes are the centroid and the two neighboring centroids inside the computational domain. For further details on the implementation of boundary conditions for the finite volume method we refer to [25, 4].

4 Numerical Results

We present numerical results for several test examples of suspended sediment and bed-load transport in shallow water flows. The main goals of this section are to illustrate the numerical performance of the unstructured finite volume method described above and to verify numerically its capabilities to solve coupled models of suspended sediment and bed-load transport in shallow water flows. In all the computations reported herein, the Courant number Cr is set to 0.8 and the time stepsize Δt is adjusted at each step according to the stability condition

$$\Delta t = Cr \min_{\Gamma_{ij}} \left(\frac{|\mathcal{T}_i| + |\mathcal{T}_j|}{2\,|\Gamma_{ij}| \max_p |(\lambda_p)_{ij}|} \right),$$

where Γ_{ij} is the edge between two triangles $\mathcal{T}_i$ and $\mathcal{T}_j$. The water density $\rho_w = 1000\ kg/m^3$ and the gravitational acceleration is fixed to $g = 9.81\ m/s^2$ for all examples presented here. Hereafter, unless otherwise stated, only second-order results are presented. Furthermore, all the computations are made on a Pentium PC with one processor of 518 MB of RAM and 166 MHz. The codes only take the default optimization of the machine, *i.e.* they are not parallel codes.

Table 1: Reference parameters used for the dam-break over erodible bed.

Quantity	Reference value	Quantity	Reference value
ρ_s	$2650\ kg/m^3$	ν	$1.2 \times 10^{-6}\ m^2/s$
p	0.4	n_b	$0.03\ s/m^{1/3}$
φ	$0.015\ m^{1.2}$	θ_c	0.045

4.1 Dam-break over erodible bed

Our first example consists of the dam-break problem in a rectangular channel with a bottom initially assumed to be flat (*i.e.* $Z(x, y, 0) = 0$). The channel is of length 50000 m, wide of 2000 m and the initial conditions are given by

$$h(x,y,0) = \begin{cases} 40\ m, & \text{if} \quad x \leq 25000\ m, \\ \\ 2\ m, & \text{if} \quad x > 25000\ m, \end{cases} \qquad u(x,y,0) = 0\ m/s, \qquad c(x,y,0) = 0.001. \tag{34}$$

The selected values for the evaluation of the present finite volume model are summarized in Table 1. At time $t = 0$ the dam collapses and the flow problem consists of a shock wave traveling downstream and a rarefaction wave traveling upstream. A similar one-dimensional test problem has been studied in [13, 33] among others. This problem has an interesting structure and will be used to verify our adaptive finite volume method namely, (i) verify if the adaptation methodology is able to compute the right speed of the hydraulic jumps and the concentration fronts, and (ii) verify that adaptive refinement is computationally cheaper than fixed meshes for a given level of solution resolution. Here, for the simulations on fixed meshes we solve the same models but without allowing adaptation.

First, we examine the accuracy of the adaptive procedure by setting the sediment particle size $d = 8\ mm$ and the Grass constant $A_s = 10^{-3}$. Figure 3 shows the adaptive meshes, water free-surface and bed-load at times $t = 1$, 2, 8 and 20 min. Here we illustrate results obtained using two-level and four-level adaptive meshes. Note that for a better comparison, only parts of the computational domain are illustrated. A simple inspection of these results shows that the bed-load and the free-surface profiles are accurately resolved along their propagation direction. Another important result is that the positions of the hydraulic jumps are not deteriorated by the multiple mesh adaptations. Needless to mention that, since the adaptive procedure is performed by monitoring the concentration of suspended sediments, refined meshes are still used for the computations although the solutions for the water free-surface are relatively smooth. Performing mesh adaptation with respect to all flow and sediment variables could be a manner to overcome this difficulties. For example, using the water depth or water surface as monitoring function the resolution in the results for the sediment transport may be improved. In order to get a closer comparison between the computed results using fixed and adaptive meshes, we present in Figure 5 cross sections of the bed and water free-surface, the water velocity and the sediment concentration at the main horizontal cross-section ($y = 1000\ m$) for the considered simulation times. Note that only parts of the computational domain are shown in these results for better visualization. It is evident that solutions computed using the coarse fixed mesh seem to be deteriorated by excessive numerical diffusion. This effect is more visible at the earlier stages of the simulation times. In contrast, the finite volume scheme using adaptive meshes tends to remove the numerical diffusion from the solutions at the local extrema. No local undershoots or overshoots have been detected in the sediment concentration in presence of steep gradients during the simulation process. Our adaptive finite volume scheme accurately approximates the solution to this sediment transport problem. In addition, the comparison with similar numerical results available in the literature [13, 33] for the one-dimensional counterpart of this test example is also satisfactory. It

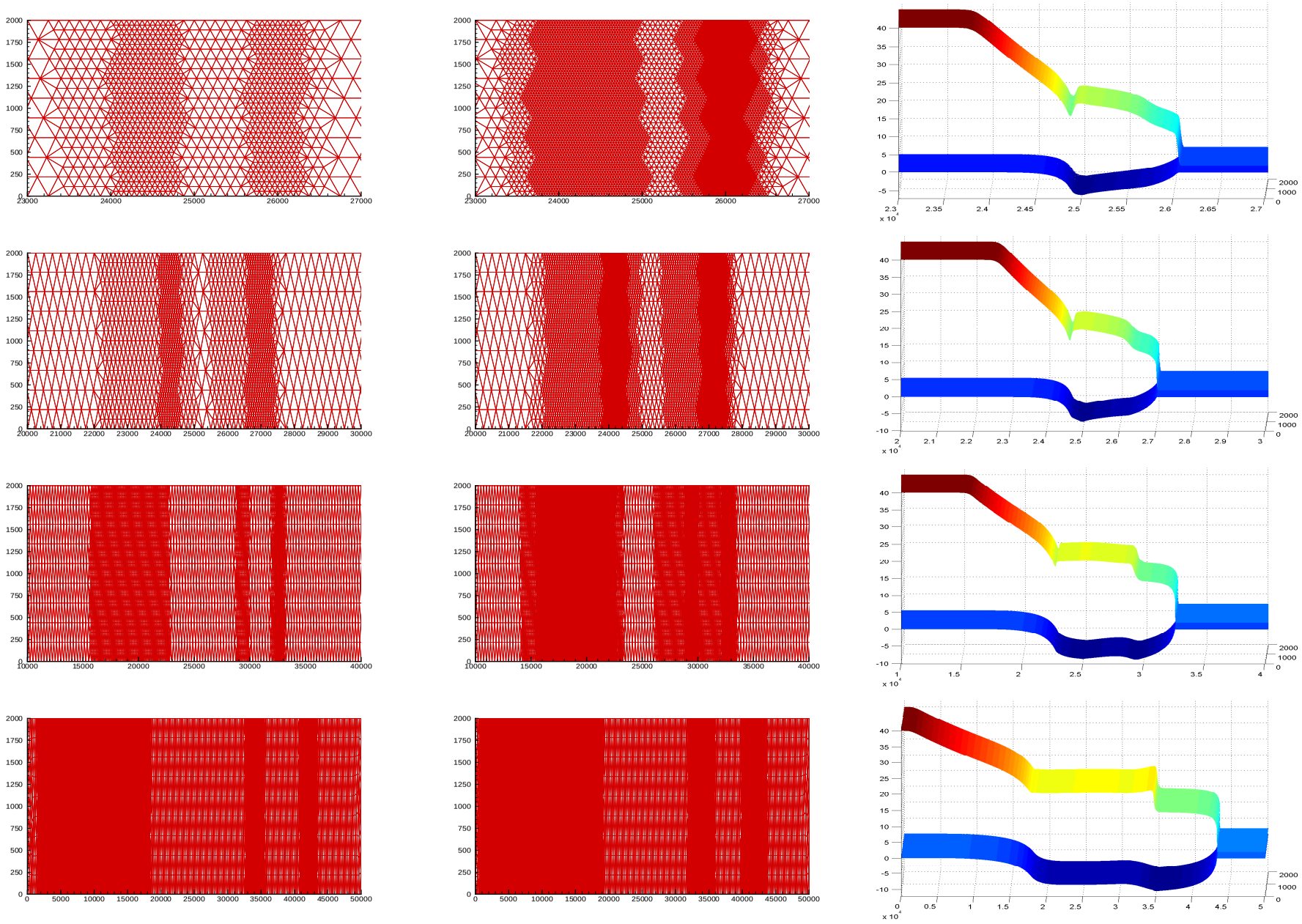

Figure 3: Two-level adaptive meshes (first column), four-level adaptive meshes (second column) and water free-surface and bed-load on the two-level adaptive meshes (third column) at different simulation times. From top to bottom $t = 1$, 2, 8 and 20 *min*.

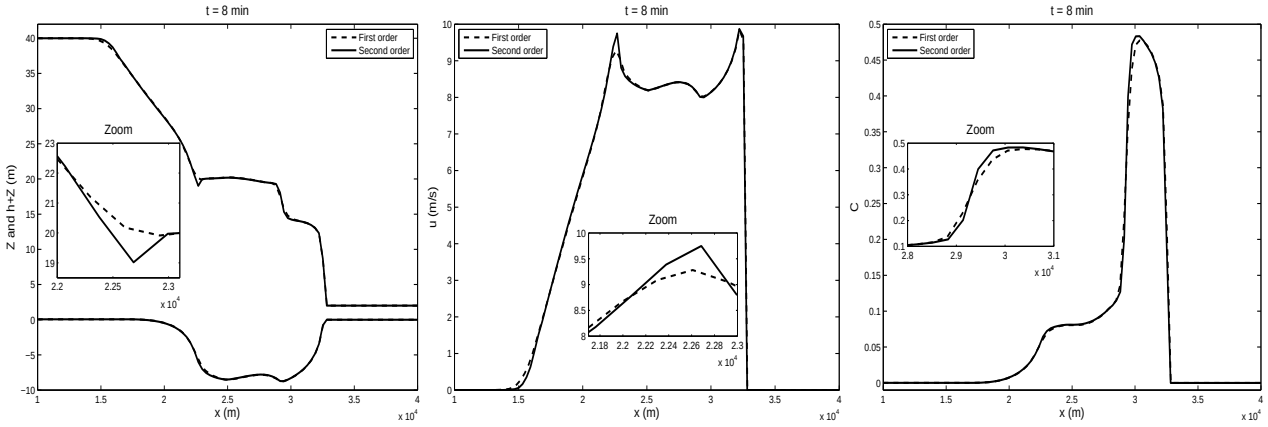

Figure 4: Comparison between the first-order and second-order results in the bed-load and water free-surface (first column), water velocity (second column) and sediment concentration (third column) using adaptive meshes at $t = 8\ min$.

should be stressed that, due to grid adaptation the final mesh at $t = 20\ min$ consists of 13292 cells only in the two-level adapted mesh compared to those associated with fixed meshes. This results in a significant reduction of the computational cost, see Table 2. Next, we compare the numerical results obtained using the first-order and the second-order reconstructions considered. In Figure 4 we present the results on the adaptive meshes for the cross sections of the bed and water free-surface, the water velocity and the sediment concentration at the main horizontal cross-section ($y = 1000\ m$) at time $t = 8\ m$. Under the considered flow and morphodynamic conditions, the first-order schemes gives very smeared solutions, compare the zoom included in the Figure 4.

To ascertain the behavior of the mesh adaptation procedure in the proposed finite volume method we summarize in Table 2 some comparative results obtained for this test example using fixed and adaptive meshes. In this table we list the mesh statistics, the maximum values of the sediment concentration, and the CPU times given in minutes. The clear indication from Table 2 is that the finite volume scheme using the four-level adaptive mesh overcomes the finite volume scheme using the two-level adaptive mesh and fixed meshes at all considered simulation times. An examination of the CPU times in Table 2 reveals that, the finite volume scheme on fixed meshes requires more computational work than its adaptive counterparts. For all the results presented, the computational effort needed for the scheme using four-level adaptive mesh is more than 12 times the one needed for the scheme using two-level adaptive mesh. It should be noted from Table 2 that the CPU time corresponding to the four-level adaptive mesh is greater than the one corresponding to the fixed fine mesh at times $t = 8\ min$ and $t = 20\ min$. This is mainly attributed to the number of times steps required to reach the targeted time in the four-level adaptive mesh and also to the time needed to refine the mesh at each level. In terms of maximum values of the sediment concentration, the results obtained by the scheme using four-level adaptive mesh are less diffusive than those obtained by other schemes. Taking all factors into account, we conclude that the adaptive finite volume scheme using two-level adaptive meshes demonstrates higher monotone and non-oscillatory properties than other fixed meshes. More importantly, a balance between efficiency and accuracy in finite volume schemes benefits the adaptive scheme using the two-level adaptive mesh, since the additional cost required for the adaptation procedure compared to the fixed meshes is minimal while the results obtained by the two-level adaptive mesh are less diffusive than those obtained using fixed meshes and roughly in the same order as those obtained using four-level adaptive mesh. Therefore, bearing in mind the slight change in the results from the four-level adaptive mesh and the two-level adaptive mesh at the expense of rather significant increase in computation time, the two-level adaptive mesh is believed to be adequate to obtain computational results almost free of grid effects for the considered sediment

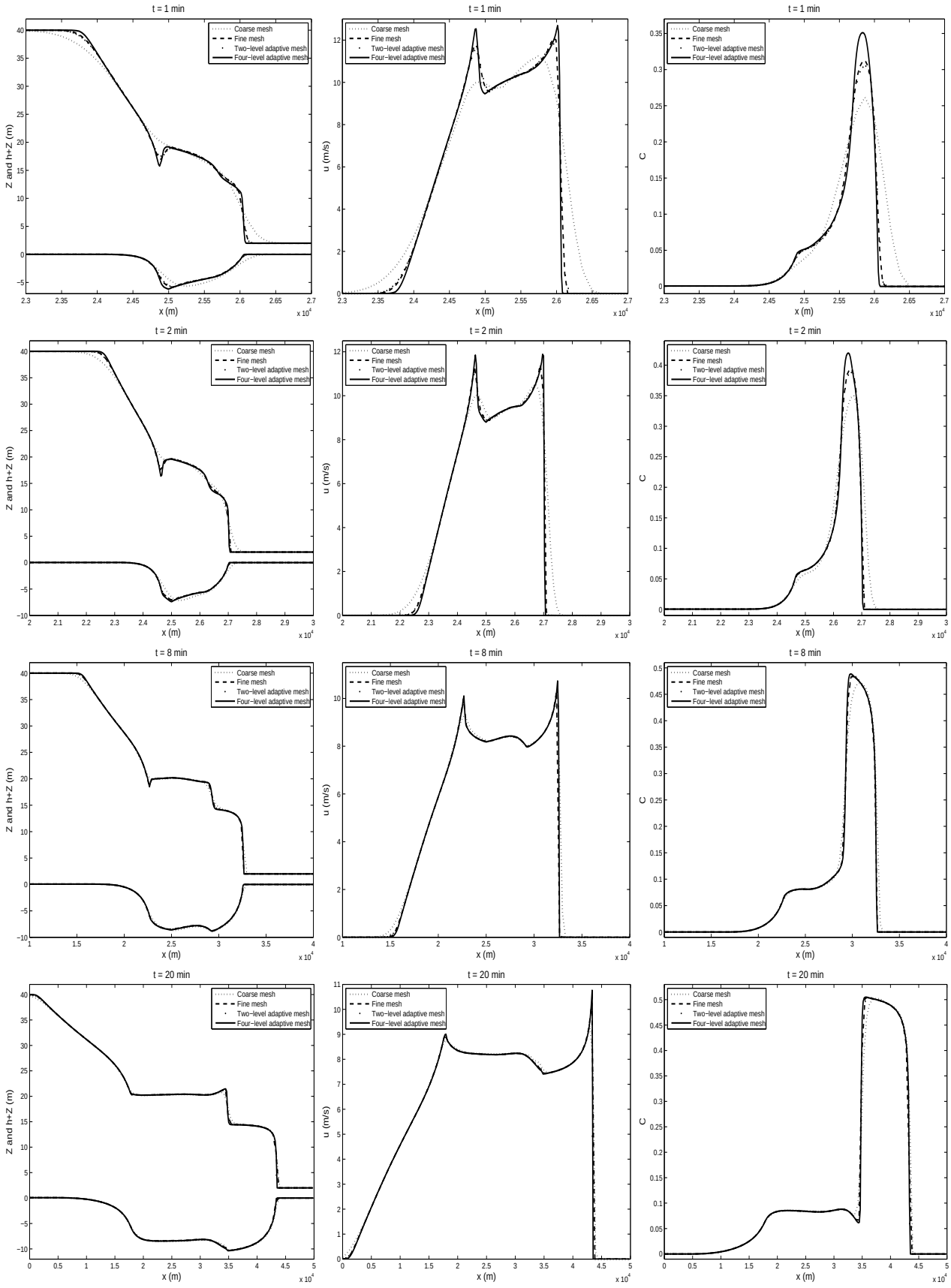

Figure 5: Comparison of different meshes in the bed-load and water free-surface (first column), water velocity (second column) and sediment concentration (third column) at four instants.

Table 2: Performance of the proposed finite volume method using adaptive, fixed and coarse meshes for the dam-break over erodible bed. The CPU times are given in minutes.

	$t = 1\ min$			
	# of elements	# of nodes	Maximum c	CPU time
Fixed coarse mesh	3592	2005	0.27	0.07
Fixed fine mesh	87968	45025	0.32	28.47
Two-level adaptive mesh	6640	3557	0.31	1.1
Four-level adaptive mesh	32494	15746	0.36	16.34

	$t = 2\ min$			
	# of elements	# of nodes	Maximum c	CPU time
Fixed coarse mesh	3592	2005	0.36	0.14
Fixed fine mesh	87968	45025	0.40	56.59
Two-level adaptive mesh	7844	4261	0.39	2.27
Four-level adaptive mesh	31290	15228	0.43	36.15

	$t = 8\ min$			
	# of elements	# of nodes	Maximum c	CPU time
Fixed coarse mesh	3592	2005	0.48	0.57
Fixed fine mesh	87968	45025	0.49	225.56
Two-level adaptive mesh	8352	4629	0.49	13.58
Four-level adaptive mesh	34614	16625	0.49	172.25

	$t = 20\ min$			
	# of elements	# of nodes	Maximum c	CPU time
Fixed coarse mesh	3592	2005	0.503	1.39
Fixed fine mesh	87968	45025	0.504	557.60
Two-level adaptive mesh	10021	5324	0.504	37.78
Four-level adaptive mesh	37528	19141	0.505	431.36

transport problem. In the sequel we show only numerical results obtained using the two-level adaptive meshes.

Now, we turn our attention to the effects of the bed sediment particle size on the water flow and sediment concentration structures. To this end we set the Grass constant $A_s = 10^{-3}$ and compute the numerical solutions using the two-level adaptive mesh for four values of the averaged diameter of the sediment particles d. In Figure 6 we present the time evolution of the bed and water free-surface, the water velocity and the sediment concentration at the four instants considered. It is evident from the presented results that dam-break flows over erodible sediment beds are highly affected by the size of sediment particles such that the finer the sediment, the greater effects bed mobility will have. It is worth remarking that, according to the equation (6), an increase of the averaged diameter of the sediment particles d yields to an increase in the settling velocity ω which is used in the deposition term (5). Thus, a weak deposition effect is expected for small sediment particles. As can be observed from these results, the erosion effects on the bed are clearly visible for small values of the bed sediment particle size. The variation of the bed sediment particle size creates a very active sediment exchange between the water flow and the bed load, and also produces a sharp spatial gradient of sediment concentration, which justify its incorporation in the momentum equations in (1). Apparently, the overall flow and sediment features for this example are preserved with no spurious

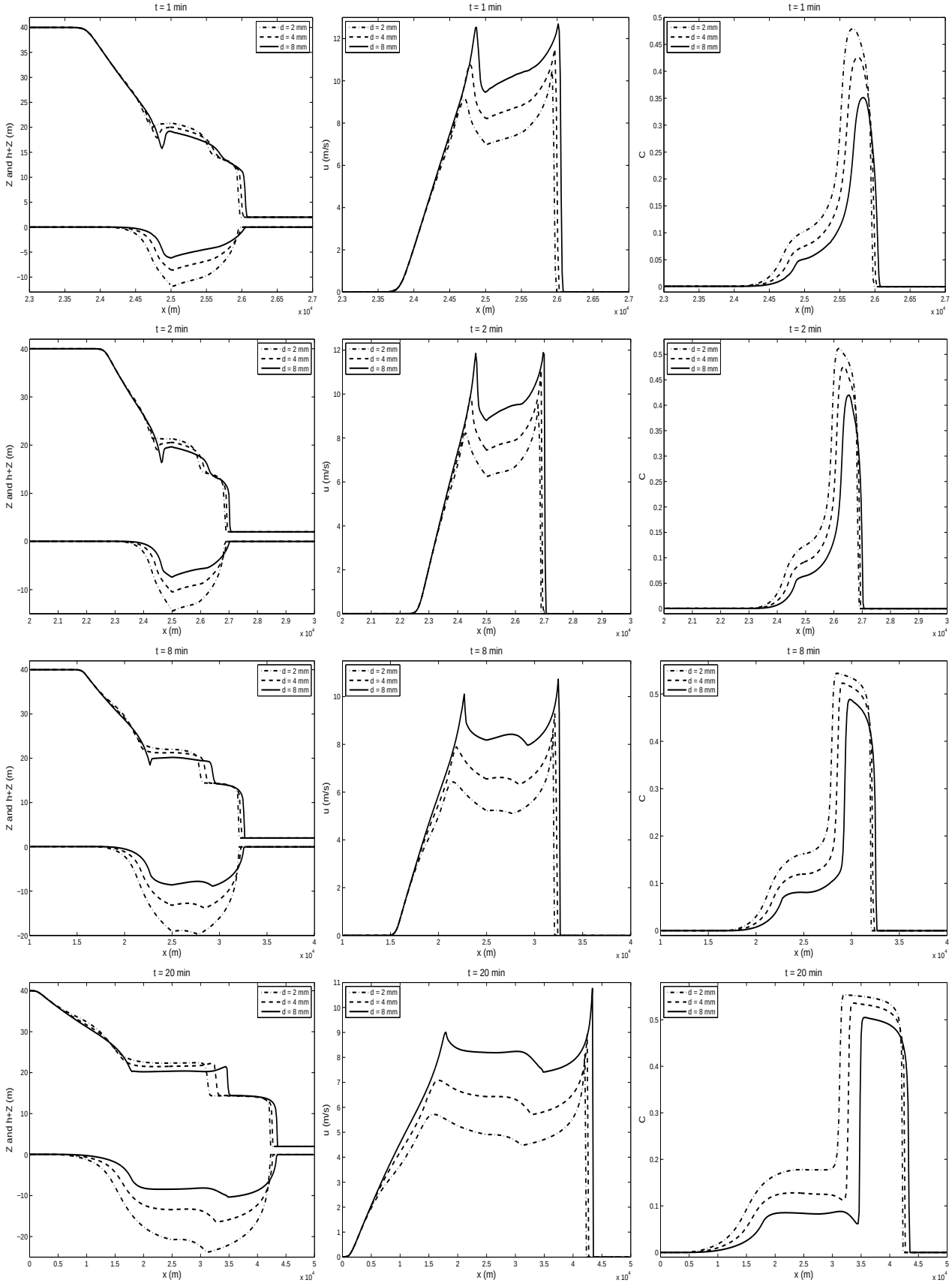

Figure 6: Comparison of different diameter values in the bed-load and water free-surface (first column), water velocity (second column) and sediment concentration (third column) at four instants.

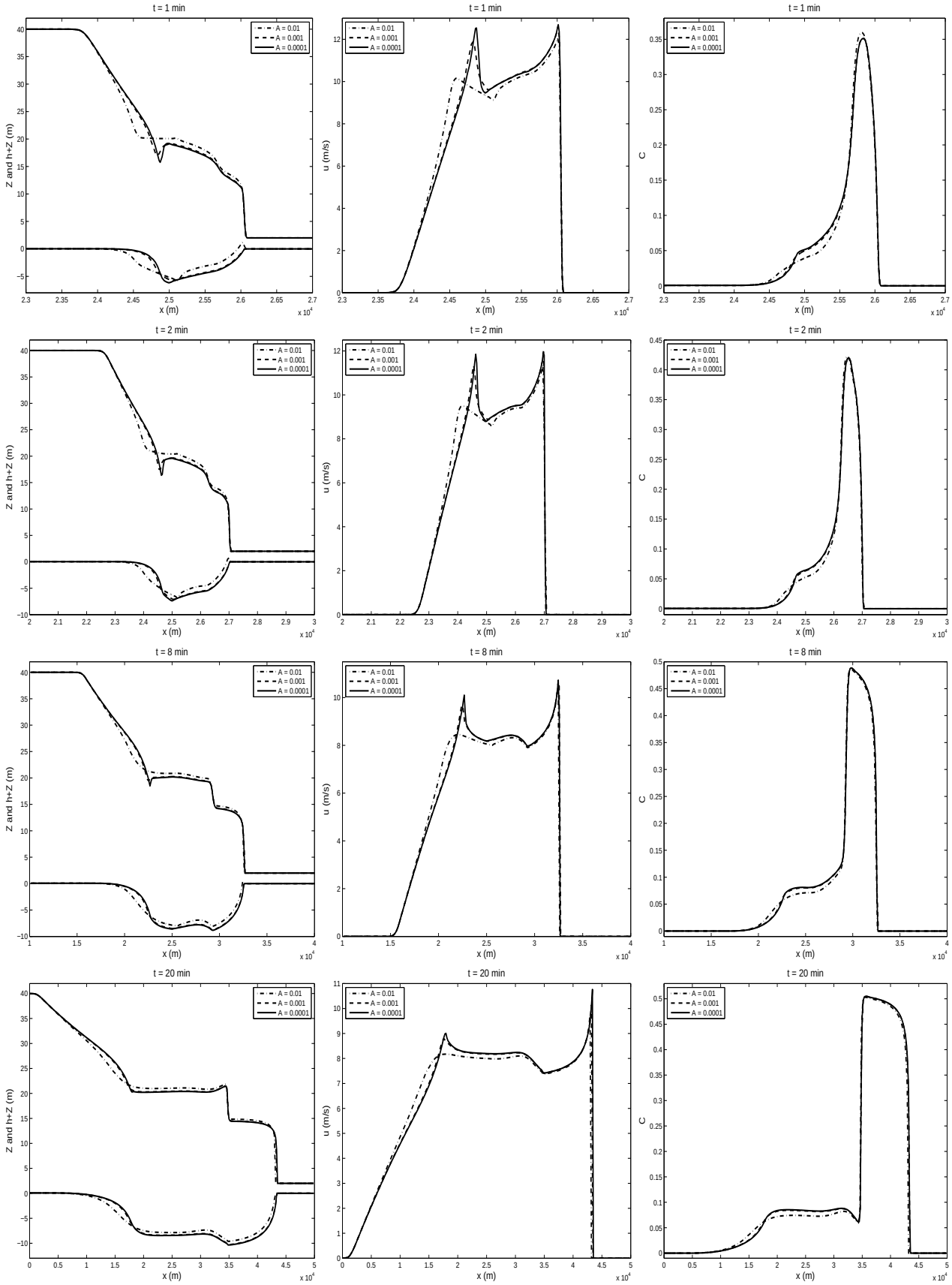

Figure 7: Comparison of different values of the Grass parameter in the bed-load and water free-surface (first column), water velocity (second column) and sediment concentration (third column) at four instants.

oscillations appearing in the results obtained using the adaptive finite volume method. Obviously, the computed results verify the stability and the discontinuity capturing properties of the proposed adaptive finite volume scheme. The obtained results using the proposed finite volume scheme are also in good agreement with those reported in [13] for the one-dimensional simulations.

Our final concern with this test example is to check the influence of the Grass constant A_s on the sediment transport results. Figure 7 exhibits the time evolution of the bed and water free-surface, the water velocity and the sediment concentration at the four instants considered for three different values of the Grass constant A_s keeping the averaged diameter of the sediment particles fixed to $d = 8\ mm$. Note that, unlike the previous one-dimensional simulations in [13, 33], the considered test case is a morphodynamical problem with movable bed resulting in the formation of strong and weak shocks, and a good numerical accuracy is required in order to capture the different phenomena present in its evolving solution. As a consequence, the later sediment transport problem is more difficult to handle; the results shown here illustrate the robustness of the proposed unstructured finite volume method. As can be seen, larger deformation has been detected in the bed-load and water free-surface solutions than those obtained for the one-dimensional simulations with $A_s = 0$ reported in [13, 33]. For the considered sediment discharge, no deposition effects on the bed have been observed for small values of the Grass constants ($A_s < 10^{-1}$). For other results, not reported in the current study, obtained for larger values of A_s (for example $A_s \geq 10^{-1}$), deposition effects may dominant the erosion and a hump is formed on the bed. The magnitude of this hump increases as the values of the Grass constant A_s become large. However, the effects of this constant on the profiles of the sediment concentration are not very strong. It seems that, for the considered sediment conditions, the sediment concentration is more sensible for the averaged diameter of the sediment particles d than for the Grass constant A_s. As can be observed from the results in Figure 7, the propagation of the water flow over the movable bottom has been accurately captured by our finite volume scheme. During the flow propagation, a hydraulic jump is formed near the initial dam place and propagates upstream. The upper front of the hump travels faster than the lower base so that the propagating bed-load creates a shock at the front after a certain time. In summary, the unstructured finite volume scheme using two-level adaptive meshes presents the most accurate numerical resolution at the discontinuity front. Similar flow and sediment features, not reported here, have been detected in the results obtained using other values for the averaged diameter of the sediment particles d. It is clear that by using adaptive meshes, high resolution is obtained in those regions where the gradients of the water depth and the sediment concentration are steep such as the moving fronts.

4.2 Partial dam-break over erodible bed

We consider a 200 m long and 200 m wide flat reservoir with two different constant levels of water separated by a dam. At $t = 0$ part of the dam breaks instantaneously. The dam is 4 m thick and the breach is assumed to be 75 m wide, as shown in Figure 8. Initially, $u(x, y, 0) = v(x, y, 0) = 0\ m/s$,

$$h(x,y,0) = \begin{cases} 10\ m, & \text{if} \quad x < 100\ m, \\ 1\ m, & \text{otherwise}, \end{cases} \qquad c(x,y,0) = \begin{cases} 0.01, & \text{if} \quad x < 100\ m, \\ 0, & \text{otherwise}, \end{cases} \qquad Z(x,y,0) = 0\ m.$$

This test example has been widely used in the literature for the evaluation of numerical methods for dam-break problems on fixed beds, see for example [3]. It should be pointed out that in most of the results reported in the literature the downstream water depth is 5 m. In our simulation this depth has been decreased to 1 m to make the erosion-deposition effects more visible. The remaining parameters used for this test example are listed in Table 3. Reflection boundary conditions are applied on all walls of the computational domain. At $t = 0$ the dam breaks asymmetrically and the water is released towards downstream to form a shock wave propagating while spreading laterally. For reasons of comparison we present numerical results for both standard dam-break over fixed bottom and dam-break over erodible bottom.

Table 3: Reference parameters used for the partial dam-break problem.

Quantity	Reference value	Quantity	Reference value
ρ_s	$2650\ kg/m^3$	ν	$1.2 \times 10^{-6}\ m^2/s$
p	0.4	n_b	$0.015\ s/m^{1/3}$
φ	$0.015\ m^{1.2}$	θ_c	0.045
d	$1\ mm$	A_s	10^{-4}

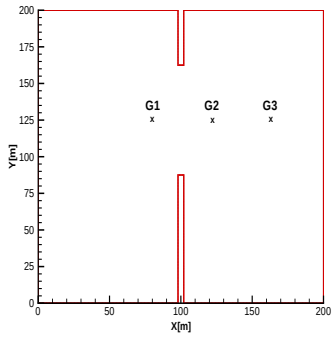

Figure 8: Computational domain for partial dam-break over erodible bed.

In Figure 9 we present the water free-surface and bed-load, the adapted meshes and snapshots of the water depth obtained for the partial dam-break over fixed bed at times $t = 2$, 4, 6 and 8 s. The results obtained for the partial dam-break over erodible bed are presented in Figure 10. We can observe in these figures that the right moving flow propagates to the downstream up and down, rarefaction wave propagates to the upstream, and two asymmetric weak vortices are developed on both sides on the breach. It is clear that the water free-surface obtained for dam-break on the erodible bed shows different features than those obtained for dam-break on the fixed bed. Notice that the erosion is more pronounced in both sides on the breach because of the large velocity field and the reflection of the wave on the upper wall. Our results are similar to other results presented in [13]. It is evident that by using adaptive meshes, high resolution is automatically obtained in those regions where the gradients of the water depth and sediment concentration are steep such as the moving fronts. Apparently, the overall flow and sediment patterns for this example are preserved with no excessive numerical diffusion in the results by finite volume method using the two-level adaptive mesh.

In order to quantify the results for this test example we display in Figure 11 cross sections at the horizontal line $y = 125\ m$ of the water free-surface and bed-load and sediment concentration at four instants shown in Figure 10. The results for the partial dam-break over fixed bed are depicted in Figure 12. Figure 13 exhibits the time evolution of the bed-load and sediment concentration at the three gauges G1, G2 and G3 presented in Figure 8. The coordinates of the gauges G1, G2 and G3 are $(80\ m, 125\ m)$, $(120\ m, 125\ m)$ and $(160\ m, 125\ m)$, respectively. It is clear that the simulated results predict the correct sediment trends at each gauge according on how far the gauge is from the dam breach. As can be observed from these results, the erosion effects on the bed are clearly visible for the considered sediment conditions. The inclusion of Exner equation in the model creates a very active sediment exchange between the water flow and the bed load, and also produces a sharp spatial gradient of sediment concentration, which justifies its incorporation in the momentum equations (10). As in the previous test example, the overall flow and sediment features for this example are preserved

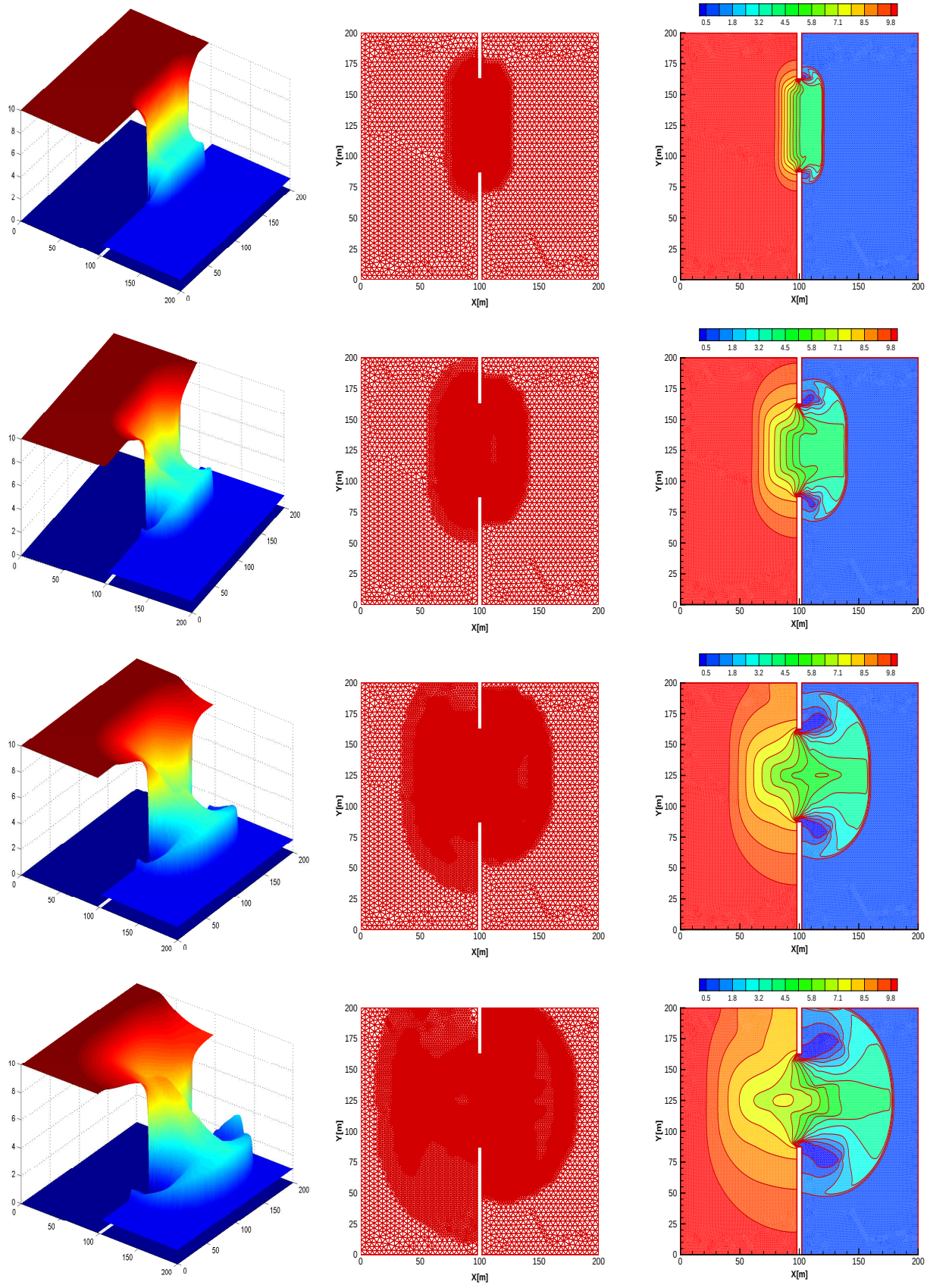

Figure 9: Water free-surface and bed-load (first column), adapted meshes (second column) and water free-surface contours (third column) for the partial dam-break over fixed bed at different simulation times. From top to bottom $t = 2$, 4, 6 and 8 s.

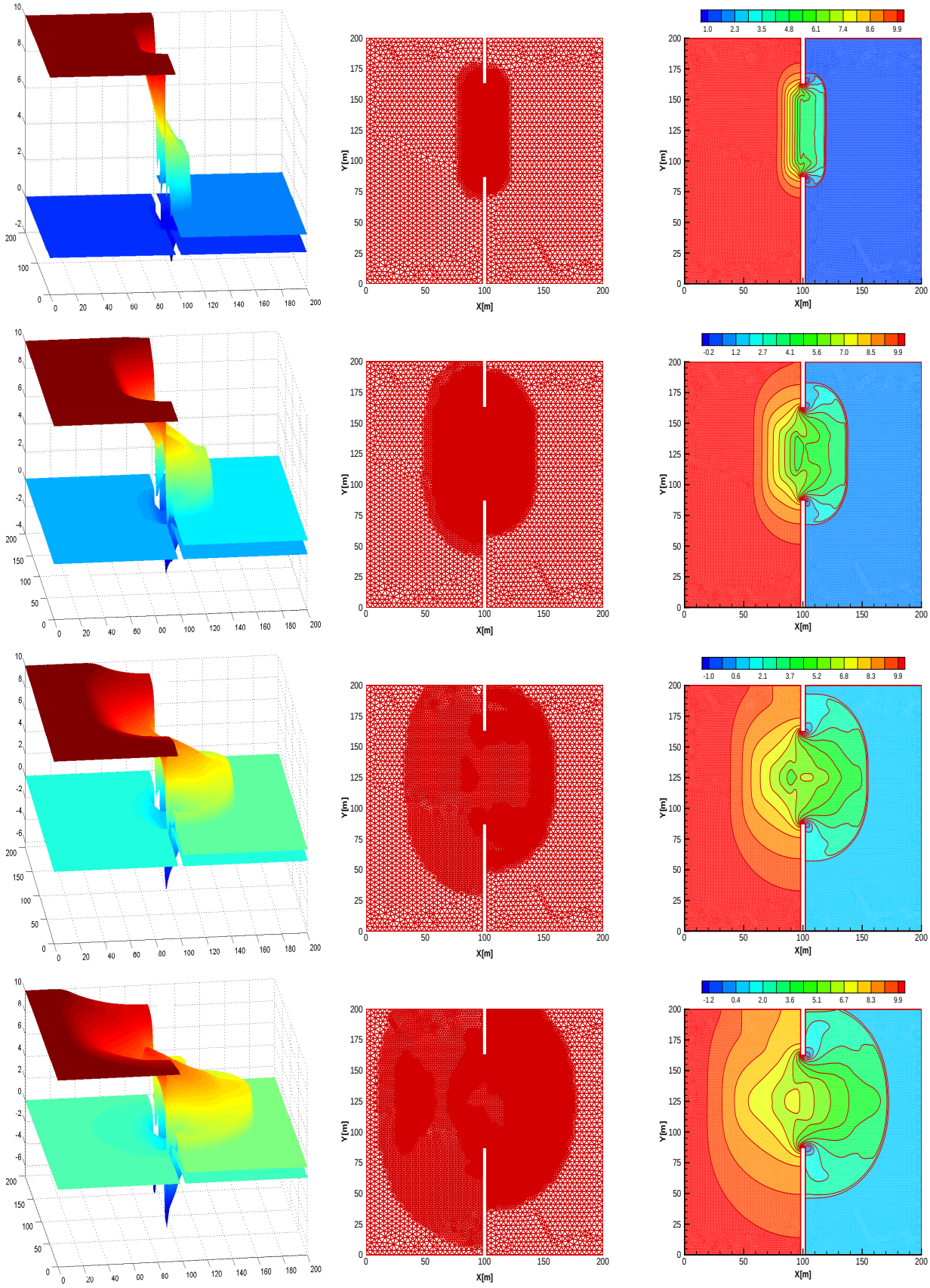

Figure 10: Water free-surface and bed-load (first column), adapted meshes (second column) and water free-surface contours (third column) for the partial dam-break over erodible bed at different simulation times. From top to bottom $t = 2$, 4, 6 and 8 s.

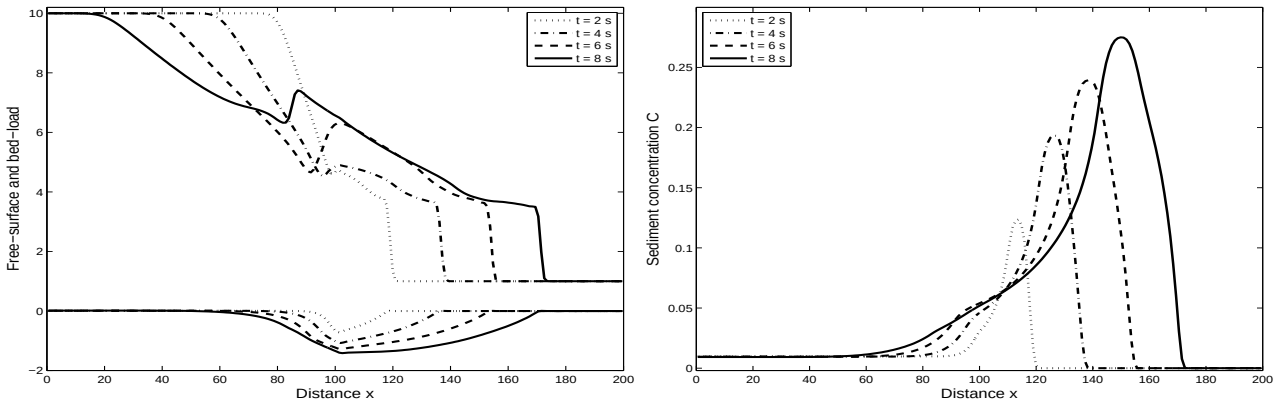

Figure 11: Cross sections at $y = 125\ m$ of the water free-surface and bed-load (left plot) and sediment concentration (right plot) at four instants.

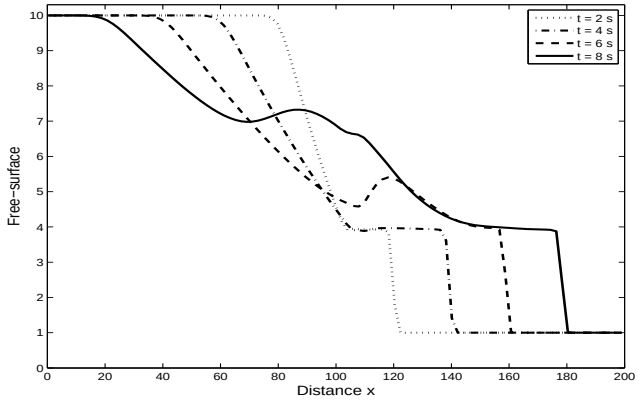

Figure 12: Cross sections at $y = 125\ m$ of the water free-surface for the partial dam-break over fixed bed.

with no non-physical oscillations appearing in the results obtained using the adaptive finite volume method.

As can be observed from these results, the partial dam-break flow over movable bed can build up a heavily concentrated wavefront, which is bounded by the wave forefront and a contact discontinuity of the sediment transport, and depresses in the long run. The bed mobility can strongly modify the water free-surface profiles, and may have considerable implications for flood predictions. As in the previous simulations, a hydraulic jump in the water free-surface is initially formed around the dam site, depresses progressively as it propagates upstream, and eventually disappears. It is evident that the movable bed can be significantly scoured and the dimensions of the scour hole are of similar order of magnitude to those of the water flow itself. Therefore the rate of bed deformation is not negligible compared to that of the flow change, characterizing the need for coupled modelling of the strongly interacting flow-sediment-morphology system as the one considered in the present work. The adaptive finite volume method performs well for this test problem.

4.3 Suspended sediment in the Nador lagoon

The Nador lagoon is located on the Moroccan eastern coast. It is a restricted lagoon of 115 km^2 (25 km by 7.5 km) and with a depth not exceeding 8 m, see Figure 14. Recently, the Nador lagoon has been the subject of many investigations on water quality, currents, flora, fauna, fishing and

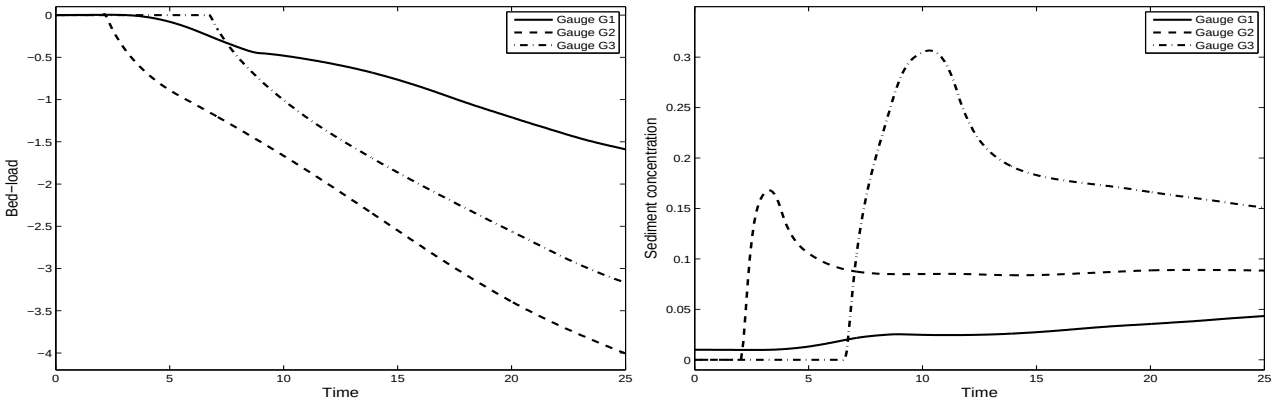

Figure 13: Time evolution of the bed-load (left plot) and sediment concentration (right plot) at the three gauges G1, G2 and G3 presented in Figure 8.

Table 4: Reference parameters used for the sediment transport in the Nador lagoon.

Quantity	Reference value	Quantity	Reference value
ρ_s	$1650\ kg/m^3$	ν	$10^{-6}\ m^2/s$
p	0.24	n_b	$0.012\ s/m^{1/3}$
φ	$0.015\ m^{1.2}$	θ_c	0.045
d	$0.5\ mm$	A_s	10^{-5}

aquaculture, see for instance [8, 29]. Most of these studies deal with the environmental aspects of the lagoon such as biological and socioeconomic impacts. However, to the best of our knowledge, there are no research studies on the numerical modelling of sediment transport in the Nador lagoon. Needless to mention that numerical studies are essential since they can quantify the interaction between sediment transport and water flow and thereafter can help to understand the evolution of the lagoon morphodynamics. Consequently, this may provide numerical tools to study the physical environment of the lagoon and to assess the development strategy reducing the flood and pollution risks in the lagoon. Certainly, numerical modelling of sediment transport in the Nador lagoon would be less costly than experimental study on the lagoon field. We consider the limited coastal region on the Nador lagoon shown in the left plot in Figure 14. The coastal boundary and the bed surface topography of the Nador lagoon are very irregular and several regions of various depths coexist in the lagoon with the minimum bathymetric values of 9 m and 8 m are localized in the center of the lagoon. As an initial bed bottom we used the reconstructed bathymetry illustrated in Figure 15. It should be pointed out that values of the topography were calibrated to cover all the unstructured meshes used at each level of refinement. Certainly, this will add some computational effort to the adaptive finite volume method. The selected values for the evaluation of the present finite volume model are summarized in Table 4. The model is started from rest and a well developed discharge of $10\ m^2/s$ is imposed at the entrance of the lagoon. This discharge corresponds to the annual mean of the Mediterranean input flux and it is also comparable to the flow generated by the main semidiurnal M_2 tide in the lagoon. For the suspended sediments we assume a small hump to be localized near the entrance of the lagoon with a maximum concentration of order 1. In this sense, the simulations are schematic, since the number, the arrangement, and the capacities of suspended sediments in the

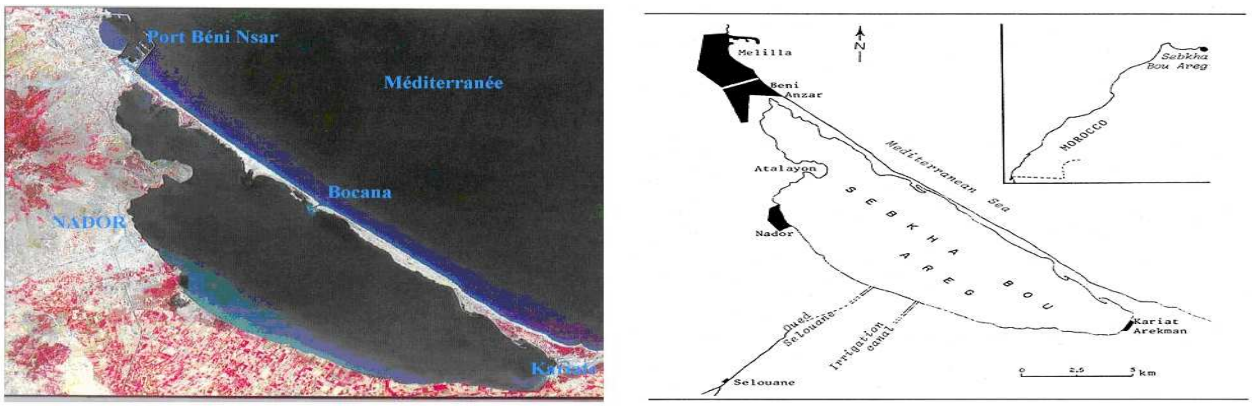

Figure 14: Location and schematic description of the Nador lagoon.

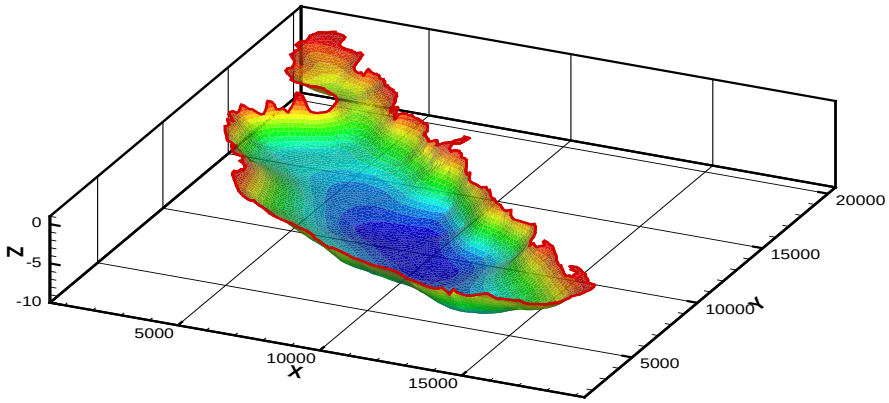

Figure 15: Reconstructed initial bottom bed used for simulations in the Nador lagoon.

Nador lagoon only partially correspond to the real situation.

In Figure 16 we present the computed results at three different times $t = 1.3$, 3 and 5 *hours* corresponding to the time required by the sediment to evolve towards the south if no wind effects are taken into account. In this figure we show the adapted meshes, velocity fields and snapshots of the sediment concentration. Notice that no adaption to the bathymetry has been performed in this test case. It is clear that the adaptive mesh procedure was able to capture the complex features of the sediment transport with a high level of accuracy. The results also show that the adaptive finite volume scheme was able to predict complex wave interactions with high accuracy and to capture sediment concentration with sharp resolution. Again, by using an adaptive grid, a high resolution can be seen in those regions where the gradients of the sediment concentration are steep such as the moving fronts. For the conditions considered, the adaptive finite volume scheme gives a shock-capturing method with very little numerical dissipation, even after long time simulations are carried out. All these features have been achieved using adaptive techniques on unstructured meshes. The presented results demonstrate that the proposed method is suited for the prediction of the transport of suspended sediments in the Nador lagoon. It should be stressed that results from the proposed sediment transport model should be compared with observations of real sea-surface flow in the Nador lagoon. However, there is no data available until now to carry out this work. Thus, at the moment we can only perform simulations and verify that results are plausible and consistent. The proposed finite volume method performs very satisfactorily on this nonlinear coupled problem. It can be clearly seen that the erosion-deposition terms play an important role in the sediment transport and change not only the transport behavior but also the flow features. In all simulations, the computed results

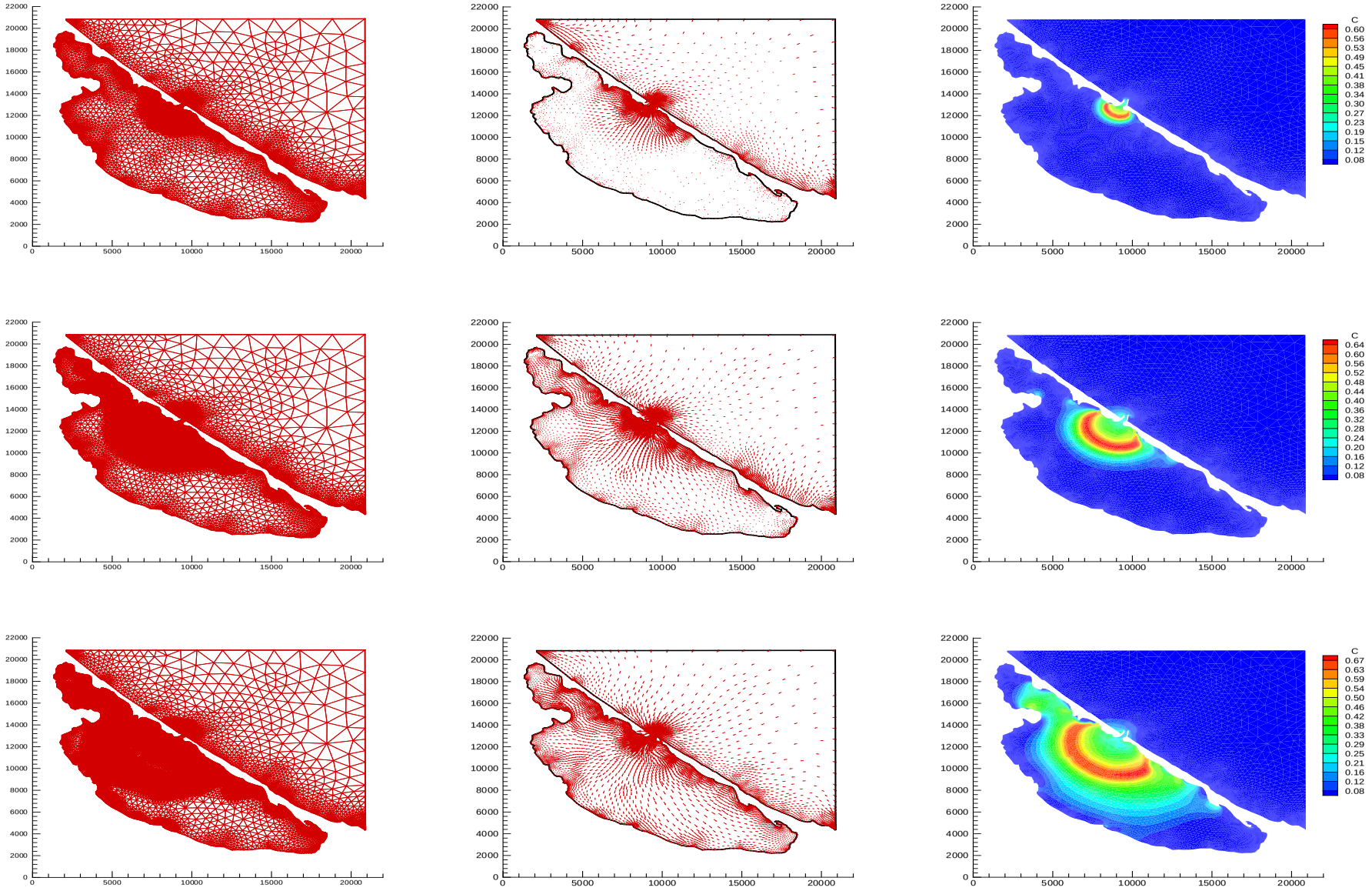

Figure 16: Adapted meshes (first column), velocity vectors (second column) and sediment concentration (third column) for sediment transport with erosion-deposition at three different simulation times. From top to bottom $t = 1.3$, 3 and 5 *hours*.

are encouraging.

As a final remark we should emphasis that a restrictive property of the Exner equation (9) equipped with the Grass formula (with $A_s \neq 0$) lies on the fact that it does not depends on a critical shear stress. Thus, using the sediment discharge (9), the movement on the bed-load begins at the same time that the water starts to move. For realistic applications in hydraulics and free-surface flows over erodible sediment beds, one should consider other formulae in the Exner equation (9) defined in terms of a critical shear stress as those proposed in [26, 28, 24] among others. It should also be noted that for these sediment discharges, it is extremely difficult to calculate analytically or approximate the eigenvalues of the coupled system. Nevertheless, the adaptive finite volume method described in this paper can be applied to these formulae by adopting the quasi-steady approach studied in [5]. This approach consists of separately solving the shallow water equations (1) and the sediment transport equation (4) to an equilibrium state keeping the bed fixed followed by a bed-load step where the bed is updated in the Exner equation (9) keeping the velocity field and water height fixed, we refer the reader to [5] for more details on this approach.

5 Conclusions

In this paper we have presented a class of finite volume methods for solving a two-dimensional coupled models of suspended sediment and bed-load transport in shallow water flows on unstructured triangular grids. The method consists of two stages which can be interpreted as a predictor-corrector procedure. In the first stage, the scheme uses the projected system of the coupled equations and introduces the sign matrix of the flux Jacobian which results in an upwind discretization of the characteristic variables. In the second stage, the solution is updated using the conservative form of the equations and a special treatment of the bed bottom in order to obtain a well-balanced discretization of the flux gradients and the source terms. To increase the accuracy of the scheme we have incorporated slope limiters along with an adaptive procedure using the sediment concentration as an error indicator. Verification of the proposed method has been carried out using test problems of two-dimensional sediment transport equations. The method exhibited good shape, high accuracy and stability behavior for all hydraulic regimes considered. The presented results demonstrate the capability of the unstructured finite volume method that can provide insight to complex suspended sediment and bed-load transport in shallow water flows.

An extension of the proposed finite volume to coupled models of suspended sediment and bed-load transport in viscous shallow water flows will be the topic of future research. The diffusion effects and tidal waves can be important in many coastal scenarios. Another planned activity will consist in a thorough comparison of different physical models for sediment discharge in the Exner equation.

Acknowledgment. The work of M. Seaïd was supported in part by Centre National de la Recherche Scientifique (CNRS) under the contract # 209821. Financial support provided by the project Mhycof, Université Paris 13 is also gratefully acknowledged.

Appendix: Determination of the sign matrix

The five eigenvalues corresponding to the projected system (17) are

$$\begin{aligned}
\lambda_1 &= 2\sqrt{-Q}\cos\left(\frac{1}{3}\theta\right) + \frac{2}{3}u_\eta, \\
\lambda_2 &= 2\sqrt{-Q}\cos\left(\frac{1}{3}(\theta+2\pi)\right) + \frac{2}{3}u_\eta, \\
\lambda_3 &= 2\sqrt{-Q}\cos\left(\frac{1}{3}(\theta+4\pi)\right) + \frac{2}{3}u_\eta, \\
\lambda_4 &= \lambda_5 = u_\eta,
\end{aligned}$$

where

$$\theta = \cos^{-1}\left(\frac{R}{\sqrt{-Q^3}}\right), \qquad Q = -\frac{1}{9}\left(u_\eta^2 + 3g(h+d)\right),$$

$$R = \frac{u_\eta}{54}\left(9g(2h-d) - 2u_\eta^2\right), \qquad d = A\xi(3\,u_\eta^2 + u_\tau^2)$$

Hence, the sign matrix in (18) is defined as

$$\operatorname{sgn}\Big[\mathbf{A}_\eta\left(\overline{\mathbf{U}}\right)\Big] = \mathcal{R}(\overline{\mathbf{U}})\operatorname{sgn}\Big[\Lambda(\overline{\mathbf{U}})\Big]\mathcal{R}^{-1}(\overline{\mathbf{U}}),$$

where $\overline{\mathbf{U}}$ is the intermediate averaged state given by (19), $\mathcal{R}(\overline{\mathbf{U}})$ and $\Lambda(\overline{\mathbf{U}})$ are respectively, the right eigenvector and the diagonal matrices reconstructed as

$$\mathcal{R}(\overline{\mathbf{U}}) = \begin{pmatrix} 1 & 1 & 1 & \gamma\bar{h} & -1 \\ \bar{\lambda}_1 & \bar{\lambda}_2 & \bar{\lambda}_3 & \gamma\bar{h}\bar{u}_\eta & -\bar{u}_\eta \\ \bar{u}_\tau & \bar{u}_\tau & \bar{u}_\tau & \gamma\bar{h}\bar{u}_\tau & -\bar{u}_\tau + \dfrac{1}{\bar{\beta}} \\ \bar{c} & \bar{c} & \bar{c} & \gamma\bar{h}\bar{c} + \bar{h} & -\bar{c} \\ \dfrac{\bar{\alpha}_1^2}{\bar{s}^2} - 1 & \dfrac{\bar{\alpha}_2^2}{\bar{s}^2} - 1 & \dfrac{\bar{\alpha}_3^2}{\bar{s}^2} - 1 & 0 & 1 \end{pmatrix},$$

$$\Lambda(\overline{\mathbf{U}}) = \begin{pmatrix} \bar{\lambda}_1 & 0 & 0 & 0 & 0 \\ 0 & \bar{\lambda}_2 & 0 & 0 & 0 \\ 0 & 0 & \bar{\lambda}_3 & 0 & 0 \\ 0 & 0 & 0 & \bar{\lambda}_4 & 0 \\ 0 & 0 & 0 & 0 & \bar{\lambda}_5 \end{pmatrix},$$

$$\mathcal{R}^{-1}(\overline{\mathbf{U}}) = \begin{pmatrix} \dfrac{\gamma_1}{\sigma_1} & -\dfrac{\bar{\alpha}_2 + \bar{\alpha}_3}{\sigma_1} & \dfrac{\bar{\beta}\bar{\alpha}_2\bar{\alpha}_3}{\sigma_1} & 0 & \dfrac{\bar{s}^2}{\sigma_1} \\ -\dfrac{\gamma_2}{\sigma_2} & \dfrac{\bar{\alpha}_1 + \bar{\alpha}_3}{\sigma_2} & -\dfrac{\bar{\beta}\bar{\alpha}_1\bar{\alpha}_3}{\sigma_2} & 0 & -\dfrac{\bar{s}^2}{\sigma_2} \\ \dfrac{\gamma_3}{\sigma_3} & -\dfrac{\bar{\alpha}_1 + \bar{\alpha}_2}{\sigma_3} & \dfrac{\bar{\beta}\bar{\alpha}_1\bar{\alpha}_2}{\sigma_3} & 0 & \dfrac{\bar{s}^2}{\sigma_3} \\ -\dfrac{\bar{c}}{\bar{h}} & 0 & 0 & \dfrac{1}{\bar{h}} & 0 \\ -\bar{\beta}\bar{u}_\tau & 0 & \bar{\beta} & 0 & 0 \end{pmatrix},$$

where $\bar{\alpha}_1 = \bar{\lambda}_1 - \bar{u}_\eta$, $\bar{\alpha}_2 = \bar{\lambda}_2 - \bar{u}_\eta$, $\bar{\alpha}_3 = \bar{\lambda}_3 - \bar{u}_\eta$, and $\bar{s} = \sqrt{g\bar{h}}$ is the wave speed calculated at the interface of control volume.

$$\gamma_1 = \bar{s}^2 - \bar{u}_\eta^2 + \bar{\lambda}_2\bar{\lambda}_3 - \bar{\beta}\bar{\alpha}_2\bar{\alpha}_3\bar{u}_\tau - \gamma\bar{c}(\bar{\alpha}_2\bar{\alpha}_3 + \bar{s}^2), \qquad \sigma_1 = -\bar{\alpha}_2\bar{\alpha}_1 + \bar{\alpha}_2\bar{\alpha}_3 - \bar{\alpha}_3\bar{\alpha}_1 + \bar{\alpha}_1^2,$$

$$\gamma_2 = \bar{s}^2 - \bar{u}_\eta^2 + \bar{\lambda}_1\bar{\lambda}_3 - \bar{\beta}\bar{\alpha}_1\bar{\alpha}_3\bar{u}_\tau + \gamma\bar{c}(\bar{\alpha}_1\bar{\alpha}_3 + \bar{s}^2), \qquad \sigma_2 = \bar{\alpha}_2\bar{\alpha}_1 + \bar{\alpha}_3\bar{\alpha}_2 - \bar{\alpha}_3\bar{\alpha}_1 - \bar{\alpha}_2^2,$$

$$\gamma_3 = \bar{s}^2 - \bar{u}_\eta^2 + \bar{\lambda}_1\bar{\lambda}_2 - \bar{\beta}\bar{\alpha}_1\bar{\alpha}_2\bar{u}_\tau - \gamma\bar{c}(\bar{\alpha}_1\bar{\alpha}_2 + \bar{s}^2), \qquad \sigma_3 = \bar{\alpha}_2\bar{\alpha}_1 - \bar{\alpha}_3\bar{\alpha}_2 - \bar{\alpha}_3\bar{\alpha}_1 + \bar{\alpha}_3^2,$$

$$\gamma = -\frac{(\rho_s - \rho_w)}{2\rho}, \qquad \bar{\beta} = \frac{2A\xi\bar{u}_\tau}{\bar{h}}.$$

References

[1] M.B. Abbott, Computational hydraulics: Elements of the theory of free surface flows, Fearon-Pitman Publishers, London, 1979.

[2] R. Abgrall, B. Nkonga, R. Saurel, "Efficient numerical approximation of compressible multi-material flow for unstructured meshes", Computers & Fluids. **32**, 571–605 (2003).

[3] F. Alcrudo, P. Garcia-Navarro, "A High Resolution Godunov-type Scheme in Finite Volumes for the 2D Shallow Water Equation", Int. J. Numer. Methods in Fluids. **16**, 489–505 (1993).

[4] F. Benkhaldoun, I. Elmahi, M. Seaïd, A new finite volume method for flux-gradient and source-term balancing in shallow water equations, Computer Methods in Applied Mechanics and Engineering, **199**, 49-52 (2010)

[5] F. Benkhaldoun, S. Sahmim, M. Seaïd, A two-dimensional finite volume morphodynamic model on unstructured triangular grids. Int. J. Num. Meth. Fluids. 63 (2010) 1296–1327.

[6] F. Benkhaldoun, I. Elmahi, M. Seaïd, "Well-balanced finite volume schemes for pollutant transport by shallow water equations on unstructured meshes", J. Comp. Physics. **226** pp:180-203 (2007).

[7] A. Bermúdez, M.E. Vázquez, "Upwind Methods for Hyperbolic Conservation Laws with Source Terms", Comput. Fluids. **23**, 1049–1071 (1994).

[8] K. Bloundi and J. Duplay, Heavy metals distribution in sediments of nador lagoon (Morocco), *Geophysical Research Abstracts*, **5**, pp. 11744, 2003.

[9] S.J. Billett, E.F. Toro, On WAF-Type Schemes for Multidimensional Hyperbolic Conservation Laws, J. Comp. Physics. **130**, 1–24 (1997).

[10] P. Brufau, M. E. Vázquez-Cendón, P. García-Navarro, "A Numerical Model For the Flooding and Drying of Irregular Domains", Int. J. Numer. Methods in Fluids. **39**, 247–275 (2002).

[11] A. Canestrelli, M. Dumbser, A. Siviglia, E.F Well-balanced high-order centered schemes on unstructured meshes for shallow water equations with fixed and mobile bed, Advances in Water Resources. **33**, 291-303, (2010)

[12] Z. Cao, G. Pender and P. Carling. Shallow water hydrodynamic models for hyperconcentrated sediment-laden floods over erodible bed. Advances in Water Resources. **29**, 546-557 (2006)

[13] Z. Cao, G. Pender, S. Wallis and P. Carling. Computational dam-break hydraulics over erodible sediment bed. J. Hydraulic Engineering. **67**, 689-703 (2004)

[14] Z. Cao and P. Carling. Mathematical modelling of alluvial rivers: reality and myth. Part I: General overview. Water Maritime Engineering. **154**, 207-220 (2002)

[15] M.J. Castro, P.G. LeFloch, Muñoz, C. Parés, Why many theories of shock waves are necessary: convergence error in formally path-consistent schemes, J. Comp. Physics. **227**, 8107–8129 (2008).

[16] N.S. Cheng, Simplified settling velocity formula for sediment particle. J. Hydraulic Engineering ASCE. 123 (1997) 149–152.

[17] I. Elmahi, F. Benkhaldoun, R. Borghi, S. Raghay, "Ignition of fuel issuing from a porous cylinder located adjacent to a heated wall: A numerical study", Combustion Theory and Modelling. **8**, 789–809 (2004).

[18] J. Fredsøe, R. Deigaard, Mechanics of Coastal Sediment Transport. *Advanced Series on Ocean Engineering - Vol. 3*, 1992.

[19] A.J. Grass, Sediment Transport by Waves and Currents. (SERC London Cent. Mar. Technol. Report No: FL29, 1981).

[20] J. Hudson, P.K. Sweby, Formations for numerically approximating hyperbolic systems governing sediment transport. *J. Scientific Computing.* **19**:225–252. (2003)

[21] G. Kesserwani, Q.A. Liang, A discontinuous Galerkin algorithm for the two-dimensional shallow water equations, Computer Methods in Applied Mechanics and Engineering. **199**, 3356-3368, (2010)

[22] J. LeVeque Randall, Numerical Methods for Conservation Laws, Lectures in Mathematics ETH Bürich, (1992).

[23] Q. Liang, A coupled morphodynamic model for applications involving wetting and drying, Journal of Hydrodynamics, Ser. B. **23**, 273-281 (2011).

[24] E. Meyer-Peter, R. Müller, Formulas for Bed-load Transport, (In: Report on 2nd meeting on international association on hydraulic structures research, Stockholm). (1948) 39–64.

[25] L.A Monthe, F. Benkhaldoun, I. Elmahi, Positivity preserving finite volume Roe schemes for transport-diffusion equations. *Comput. Methods Appl. Mech. Engrg.* 1999; **178**:215–232.

[26] D. Pritchard, A.J. Hogg, On sediment transport under dam-break flow. *J. Fluid Mech.* 2002; **473**:265–274.

[27] P.L. Roe, Approximate Riemann Solvers, Parameter Vectors and Difference Schemes, J. Comp. Physics. **43**, 357-372 (1981).

[28] G. Rosatti, L. Fraccarollo, A well-balanced approach for flows over mobile-bed with high sediment-transport. *J. Comput. Physics* 2006; **220**:312–338.

[29] F. Ruiz, M. Abad, M. Olias, E. Galán, I. González, E. Aguilá, N. Hamoumi, I. Pulido and M. Cantano, The present environmental scenario of the Nador lagoon (Morocco). *Environmental Research*, **102**, pp. 215–229, 2006.

[30] S. Sahmim, F. Benkhaldoun, F. Alcrudo, A Sign Matrix Based Scheme for Quasi-Hyperbolic Non-Homogeneous PDEs with an Analysis of the Convergence Stagnation Problem, J. Comput. Phys. **226**, 1753-1783 (2007).

[31] S. Soares-Frazão, Y. Zech, HLLC scheme with novel wave-speed estimators appropriate for two-dimensional shallow-water flow on erodible bed, Int. J. Numer. Methods in Fluids. **66**, 1019–1036 (2011).

[32] R.L. Soulsby: Dynamics of marine sands, a manual for practical applications. HR Wallingford, Report SR 466 (1997)

[33] G. Simpson and S. Castelltort. Coupled model of surface water flow, sediment transport and morphological evolution. Computers & Geosciences. **32**, 1600-1614 (2006)

[34] G. Strang. On the Construction and the Comparison of Difference Schemes. SIAM J. Numer. Anal. **5**, 506-517 (1968)

[35] E.F. Toro, "Shock-Capturing Methods for Free-Surface Shallow Waters", Wiley Chichester 2001

[36] C.Y. Yang,: Sediment Transport: Theory and Practice. McGraw-Hill, New York (1996)